13

STRUCTURE AND ENERGY OF HOMOPHASE INTERFACES

In our discussion of homophase interfaces, we first examine the structure and properties of grain boundaries, which are the most common planar (two-dimensional) defects in materials. We then look at special planar boundaries, such as twin interfaces and stacking faults.

13.1. GRAIN BOUNDARY ENERGY

As in the previous parts, we begin our discussion of grain boundaries by first examining some typical values of the grain boundary energy. Average grain boundary energies can be determined by annealing metal or alloy wires at high temperature in vacuum and measuring the dihedral angle that forms where a grain boundary intersects the surface, as illustrated in Figure 13.1. This method is called the thermal-grooving technique [24], and the dihedral angle can be measured by optical interferometry or by scanning electron microscopy (SEM). In a manner similar to the contact angle in Figure 7.1, the balance of the interfacial energies at the triple point in Figure 13.1 yields the equation

$$\gamma_{gb} = 2\gamma^{SV} \cos(\theta^{SV}/2), \tag{13.1}$$

where γ_{gb} is the grain boundary energy, γ^{SV} is the surface energy for the solid–vapor case and θ^{SV} is the dihedral angle defining the groove. Measurement of θ^{SV} allows the ratio of γ_{gb}/γ^{SV} to be determined, and, if γ^{SV} is known, then the magnitude of γ_{gb} can also be found.

Table 13.1 lists the interfacial energy ratio γ_{gb}/γ^{SV} for several f.c.c. metals. It can be seen that the ratio γ_{gb}/γ^{SV} varies from approximately 0.25–0.35 for the f.c.c. metals. A more extensive review by Murr [24] shows that this is typical for many metals and alloys. We used these ratios and the data for the surface energies of the

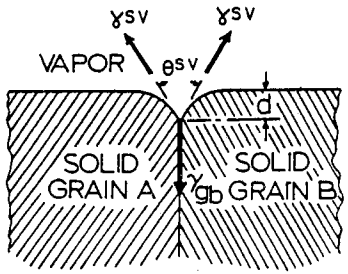

Figure 13.1. Thermal groove profile for grain boundary–surface equilibrium involving evaporation–condensation. The groove depth is d. From [24].

corresponding solid–vapor interfaces to calculate the grain boundary energies according to Eq. (13.1); these are also shown in Table 13.1. If we examine the trend among silver, gold and copper, the three f.c.c. metals that we often used in Part II, we see that silver and gold have very similar grain boundary energies, whereas the grain boundary energy of copper is significantly higher. This is not too different from our ranking of the solid surface energies, although the value for gold is a little low. However, if the grain boundaries were truly average and there were no surface contamination effects, the grain boundary energies should scale with the solid surface energies shown in Table 3.3, provided the grooves formed by the same thermal grooving mechanism. The fact that they do not indicates that such data should be interpreted with caution. We see in subsequent sections that grain boundary energies are highly dependent on orientation.

The temperature coefficients of the grain boundary energy have been measured for only a small number of metals and alloys, and these are also shown for the f.c.c. metals in Table 13.1. Examples of the grain boundary energy versus temperature for nickel and stainless steel are shown in Figure 13.2. The temperature coefficients for grain boundaries are negative and appear proportionally smaller than those for solid surface energies, as given in Eq. (3.15).

Table 13.1. Average grain boundary energies for various f.c.c. metals

Metal	γ_{gb}/γ^{SV}	Temperature (°C)	γ_{gb} (mJ/m^2)	$d\gamma_{gb}/dT$ (mJ/m^2·°C)
Al	0.23	450	324	–0.12
Cu	0.34	950	625	–0.10
Ni	0.38	1060	866	–0.20
Ag	0.25	950	375	–0.10
Au	0.27	1000	378	–0.10
Pt	0.29	1300	660	–0.18

Source: From [24].

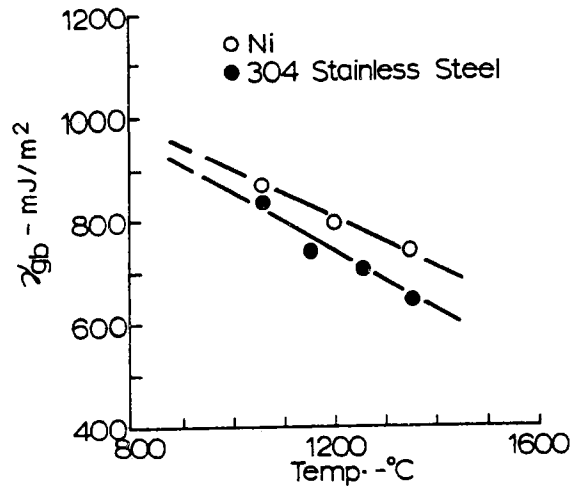

Figure 13.2. Variation of grain boundary energy γ_{gb} for nickel and stainless steel with temperature below the melting point. From [24].

13.2. GRAIN BOUNDARY STRUCTURE

A number of different analytical models have been proposed to describe the structure and properties of grain boundaries. The models vary both in their approach and degree of sophistication. Several of the more important ones are discussed in the following sections. The discussion progresses in approximate order of historical development, beginning with the early interpretation of low-angle grain boundaries in terms of dislocation networks by Read and Shockley [25,26] and closing with recent comprehensive atomistic simulations by Wolf and Merkle [2,7]. Most of the analytical treatments that have been developed for grain (homophase) boundaries can be similarly applied to interphase (heterophase) interfaces. To emphasize the generality of the methods and to avoid duplication in Chapter 14 on heterophase interfaces, extension of the treatments from homophase to heterophase interfaces is included with the discussion of each model in this chapter on homophase interfaces.

13.2.1. Dislocation Models

Symmetrical Tilt Grain Boundary One of the simplest types of grain boundaries to visualize is a symmetrical tilt boundary, where two grains on either side of the boundary are related by symmetrical rotations about an axis lying in the boundary plane. Figure 13.3 illustrates such a boundary in a simple cubic structure, where the boundary was formed by joining two crystals having surfaces rotated from a cube plane by $\pm\theta/2$ about a <100> axis. When the two surfaces are joined, the ledges on them become edge dislocations of Burgers vector **b**, where the magnitude of the

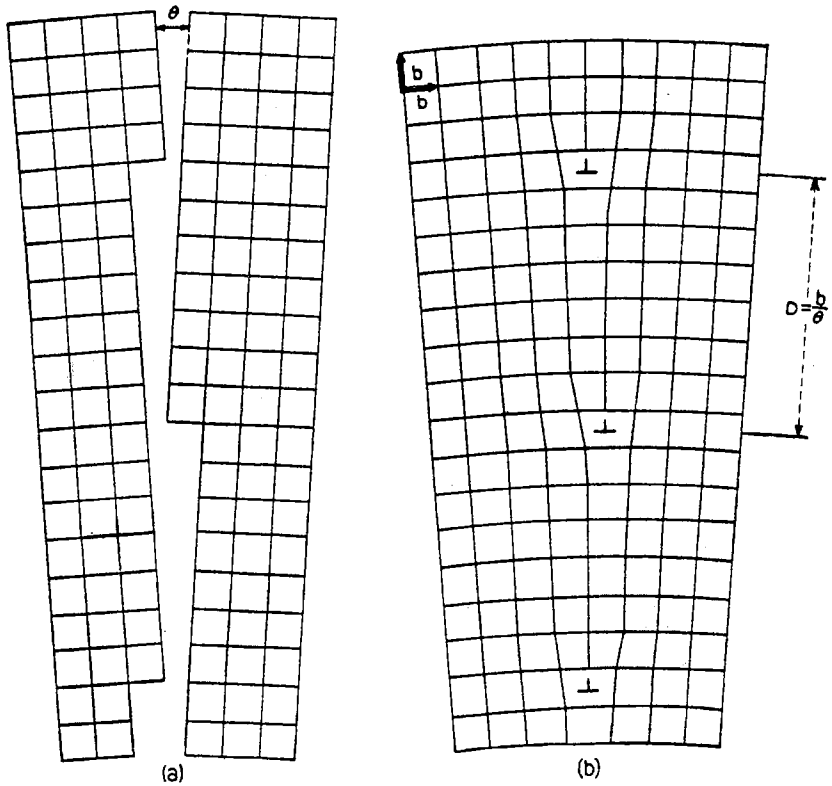

Figure 13.3. Symmetrical-tilt grain boundary in a simple cubic crystal. The plane of the figure is parallel to a cube face and normal to the axis of rotation of the two grains. (a) The two grains are rotated by an angle θ and (b) joined to form a bicrystal (grain boundary). From [25].

Burgers vector $b = |\mathbf{b}|$ is equal to the ledge height h_l. A similar tilt boundary for an atomistic model with {111} surfaces and a <110> tilt axis was previously shown in Figure 12.2b. Joining the crystals in Figure 13.3b requires only elastic strain except where planes of atoms terminate at the boundary in an edge dislocation, indicated by the symbol ⊥. Here the atoms have fewer nearest neighbors than in the bulk.

From the geometry in Figure 13.3b, the number of edge dislocations per unit length in the grain boundary is given by

$$\frac{1}{D} = \frac{2\sin(\theta/2)}{b} \tag{13.2a}$$

or when θ is small by

$$\frac{1}{D} \cong \theta/b, \tag{13.2b}$$

where D is the distance between the grain boundary dislocations. This boundary constitutes a wall of dislocations and Read and Shockley [26] have calculated the energy of such an array, situated in an infinite medium of shear modulus μ and Poisson's ratio ν. An important consideration in their analysis is that each dislocation has an elastic strain energy per unit length $E_\perp$ that varies according to the spacing between the dislocations D. Thus, the elastic strain energy must be integrated as a function of θ to find its angular dependence. The grain boundary energy γ_{gb} is then given by the product of the energy per unit length of the dislocations $E_\perp$ times the density of the dislocations as $\gamma_{gb} = E_\perp(1/D) = E_\perp(\theta/b)$. The resulting expression for the energy per unit area of the grain boundary γ_{gb} is given by

$$\gamma_{gb} = E_0\theta(A_0 - \ln\theta), \tag{13.3a}$$

where

$$E_0 = \frac{\mu b}{4\pi(1-\nu)} \quad \text{and} \quad A_0 = 1 + \ln\left(\frac{b}{2\pi r_0}\right) \tag{13.3b}$$

and r_0 represents the core energy of a single boundary dislocation. The grain boundary energy γ_{gb} has units of energy per unit area (mJ/m^2).

The term A_0 in parentheses in Eq. (13.3) depends on the total core energy of the dislocation per unit area of the boundary, whereas the ln θ term accounts for the elastic energy of the boundary. The first term represents a constant energy per dislocation, and it leads to an increase in the energy that is proportional to the density of the dislocations. The second term decreases as θ increases because the stress fields of the dislocations overlap and cancel one another as D decreases. Hence, this equation can only be applied to boundaries having a small angle of tilt (θ ~ 10–15 degrees) such that the cores of the dislocations do not overlap. Such boundaries are referred to as low-angle tilt boundaries. Also note that the Read–Shockley equation shows that it is energetically favorable for two low-angle tilt boundaries with misorientations θ_1 and θ_2 to combine to form a single tilt boundary with angle $(\theta_1 + \theta_2)$. In addition, differentiation of Eq. (13.3a) predicts that γ_{gb} has a maximum at $\theta = \exp(A_0 - 1)$.

A plot of Eq. (13.3a) is shown in Figure 13.4, where it is seen that the cusp at θ = 0 is very sharp when the boundary disappears; that is, $d\gamma_{gb}/d\theta$ becomes infinite at θ = 0. This is because a long-range stress field is established when an isolated ledge is pressed into another crystal to make a grain boundary dislocation. Thus, the energy of a tilt boundary rises steeply as its angle increases from zero because the strain field of each dislocation spreads out to very large distances in the crystal when they are widely separated. This contrasts with the much shallower cusps found at solid–vapor interfaces, where the energy is localized at the ledges and reverts to the surface energy of the singular surface when θ = 0. In the tilt boundary, the slope becomes less steep as the stress fields approach one another and begin to cancel, and eventually the slope becomes almost constant at high tilt angles. Using this dislocation concept of a low-angle symmetrical tilt grain boundary, we see that the boundary has many characteristics that are similar to vicinal solid–vapor interfaces,

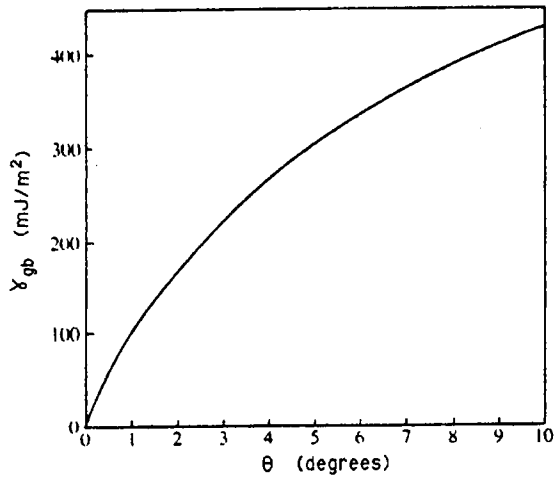

Figure 13.4. Energy of a tilt grain boundary as a function of tilt angle θ with E_0 = 1450 mJ/m^2 (appropriate for copper) and A_0 = 0. Reprinted from [31] by permission of Addison-Wesley Longman Publishing Company, Inc.

such as a low energy cusp at low tilt angles, but that the nature of the elastic strains are an additional important part of this solid–solid interface.

Although the dislocation model was developed for low-angle grain boundaries where the dislocation cores are well-defined and surrounded by regions of relatively well-bonded crystal, it can be extended on a purely geometrical basis to high-angle boundaries. If the angular tilt is continued beyond the low-angle regime, the energy is expected to increase only slightly as the density of dislocation cores increases and shallow cusps are expected to occur at particular angles of tilt where the dislocations are uniformly spaced. According to the formula for a simple cubic lattice, this occurs when cot (θ/2) = $2n$, where n is an integer. For example, when cot (θ/2) = 14, there is one dislocation on every seventh cube plane, or when cot (θ/2) = 2 (or θ = 53°) the structure is particularly simple and forms a twin plane, as shown in Figure 13.5. In this case, the twin plane is (210), and the atoms in the twin boundary lie on the lattices of both grains. The density of atoms on the boundary plane is high, and the resulting grain boundary energy is low. This type of boundary is sometimes referred to as a special high-angle grain boundary.

A uniform dislocation spacing in a high-angle grain boundary such as in Figure 13.5 only results when the dislocation spacing is an integral number of lattice planes terminating at the boundary as illustrated in Figure 13.6a. When the misorientation changes in a symmetrical high-angle tilt grain boundary, the dislocation spacing ideally varies from uniform to nonuniform, as shown schematically in Figure 13.6. A nonuniform grain boundary can be described as consisting of a uniform dislocation array and a superimposed nonuniform array. For example, the nonuniform 60° symmetrical-tilt boundary in Figure 13.6b can be described as a 53° tilt

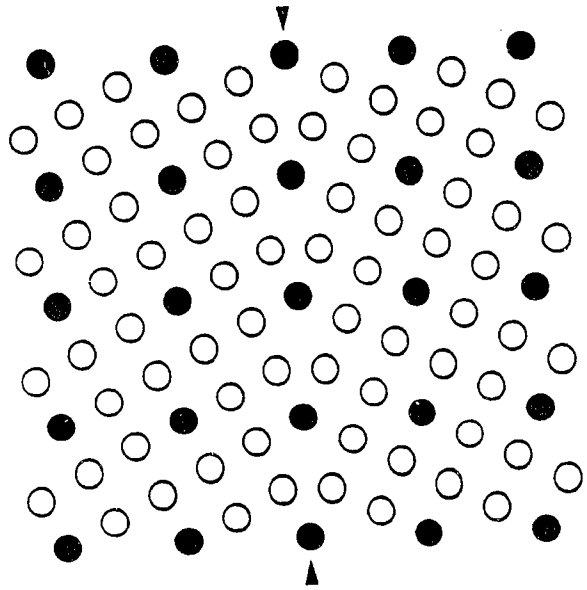

Figure 13.5. High-angle tilt boundary of good fit. The (210) twin boundary (arrows) is normal to the plane of the figure and the dark circles represent atoms that lie on points of lattices of both grains. From [27].

boundary (Fig. 13.6a) with a superimposed 7° tilt boundary. With further tilt to 62°, the boundary once again becomes uniform but with a higher dislocation density, as illustrated in Figure 13.6c. The variation in energy of such symmetrical tilt boundaries has been calculated assuming that the energy consists of the sum of the two superimposed dislocation arrays and is shown in Figure 13.7. Note the cusp at a 53° tilt in Figure 13.7 corresponding to the (210) boundary in Figure 13.5.

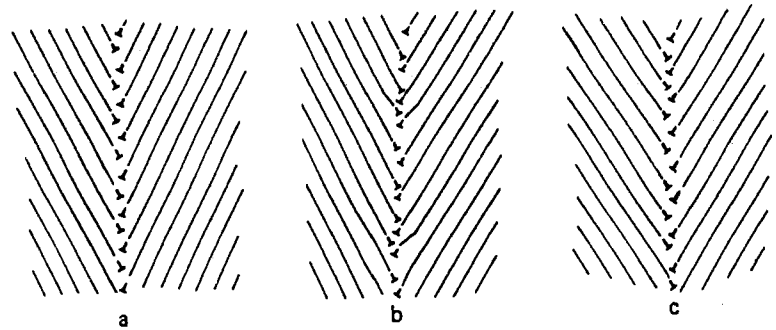

Figure 13.6. Dislocation models of symmetrical tilt boundaries showing the variation in uniformity of the spacing with misorientation angle: (a) 53°, (b) 60° and (c) 62° misorientation. From [24].

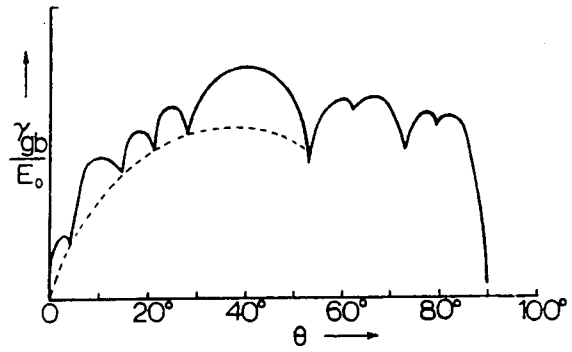

Figure 13.7. Relative grain boundary energy versus misorientation angle for symmetrical tilt boundaries which vary in uniformity of dislocation arrays. Cusps correspond to uniform arrays. From [24,28].

Both atomistic calculation and experimental data suggest that the cusps shown in Figure 13.7 exist. For example, Figures 13.8a and b compare calculated and experimental data for the grain boundary energies of symmetrical <100> and <110> grain boundaries in f.c.c. aluminum. The calculations were performed using a Morse potential for aluminum, similar to the 6–12 Lennard–Jones potential that we have used frequently in this book. The atomistic calculations are similar to but more realistic than the pure dislocation model described above, because they allow for atomic relaxations and translations along the boundary that are not included in the dislocation model. The experimental and calculated curves in Figure 13.8 are in generally good agreement, although the small cusps associated with the <100> tilt boundary in Figure 13.8a are not evident experimentally in Figure 13.8b due to their relatively small magnitude compared to the scatter in the data. In contrast, the large cusps at about 70° and 129° in Figures 13.8c and d are clearly evident, and these are associated with low-energy {111} and {113} twin boundaries which are possible with rotation about the <110> axis. The {111} twin boundary was shown previously in Figure 12.1. Note that the magnitudes of the calculated grain boundary energies in Figure 13.8 are about twice the measured values given in Table 13.1.

We look at atomistic calculations of grain boundary structures in depth in a subsequent section, but it is worth noting that plots like Figures 13.7 and 13.8 resemble the γ^{SV} plots seen previously in Chapters 3 and 4. A slightly different type of plot could also be obtained by maintaining a constant angle of tilt between two crystals and varying the grain boundary plane. This would be very much analogous to the γ^{SV} plots for solid–vapor interfaces in Section 3.4. Certain orientations of the plane will have particularly low energies, and these will likely become facet planes of enclosed crystals. An example of this is illustrated below in our discussion of the asymmetrical tilt boundary.

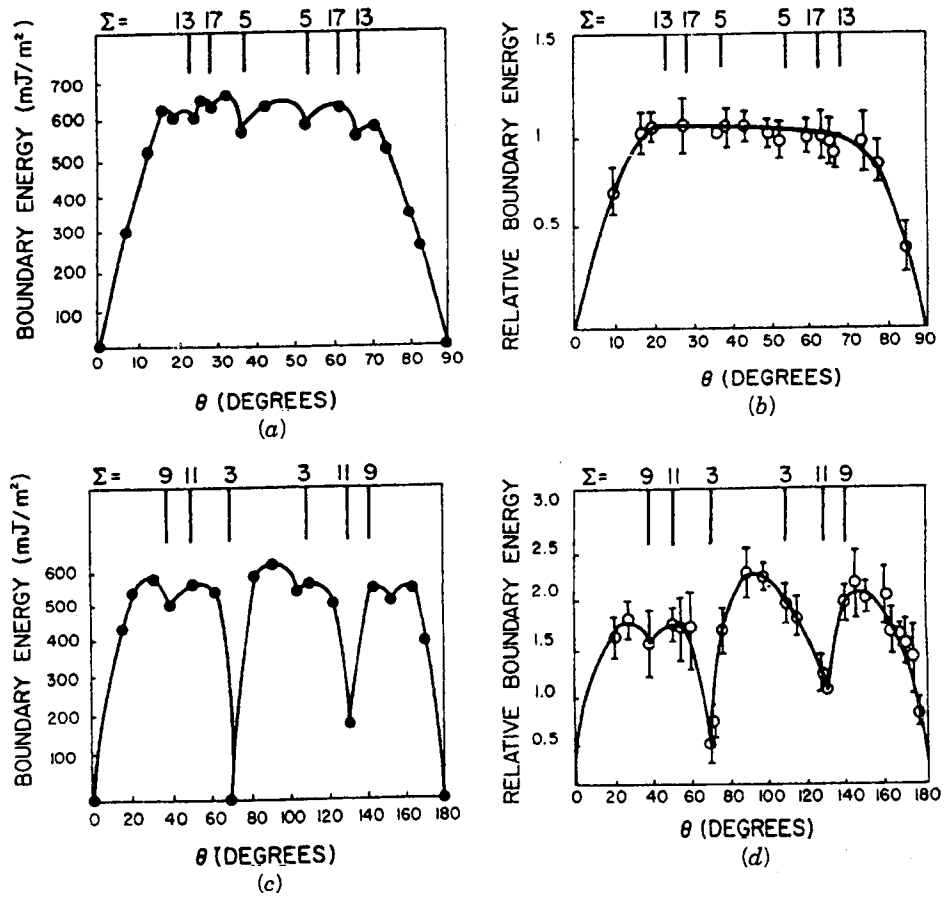

Figure 13.8. (a,c) Calculated and (b,d) experimental grain boundary energies as a function of misorientation angle for (a,b) <100> and (c,d) <110> symmetrical tilt boundaries in aluminum. Reprinted from [29,30] with kind permission from Elsevier Science-NL, Amsterdam, The Netherlands.

Asymmetrical Tilt Grain Boundary The tilt boundary in Figure 13.3b can be turned out of its symmetrical orientation by rotating it about the tilt axis through an angle Φ, as illustrated in Figure 13.9. In this case, the angle Φ is the angle between the boundary plane and the mean <100> direction of the two grains. The boundary makes an angle of $\Phi + \theta/2$ with the [100] direction in one grain and angle of $\Phi - \theta/2$ with the [100] direction in the other grain. Figure 13.3 is thus a special case where $\Phi = 0$ or 90°. When the boundary becomes asymmetrical, edge dislocations with extra planes that are normal to those of the original set are introduced, and it can be shown that their spacing [25] is given by

$$D_2 = \frac{b_2}{\theta \sin \Phi}, \tag{13.4a}$$

whereas the spacing of the original set is reduced to

$$D_1 = \frac{b_1}{\theta \cos \Phi}. \tag{13.4b}$$

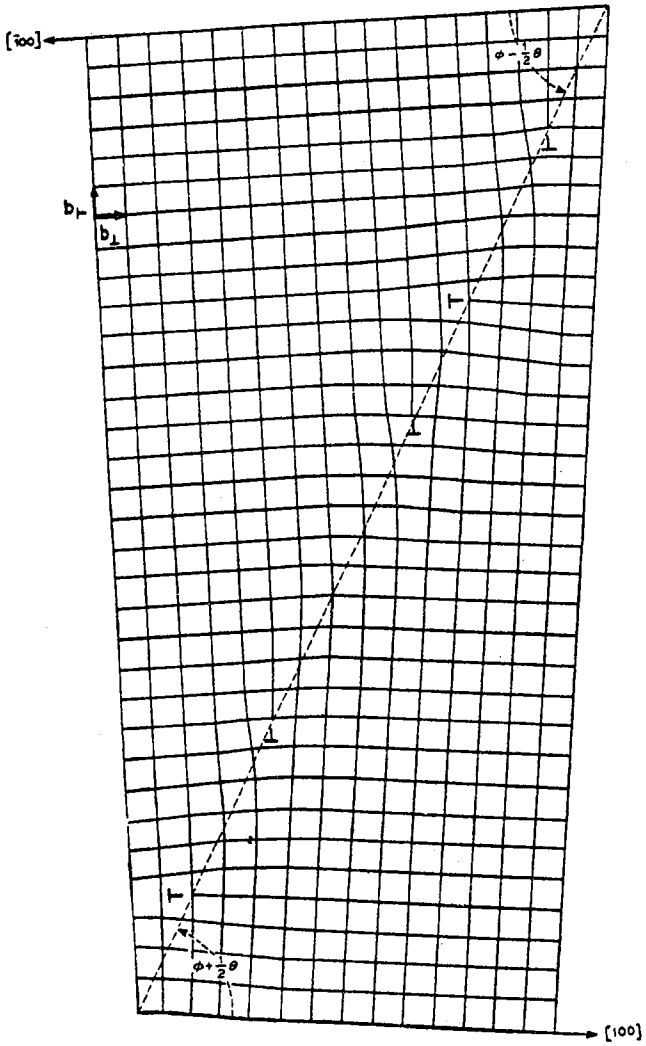

Figure 13.9. The same grain boundary as in Figure 13.3 except that the plane of the boundary makes an arbitrary angle Φ with the mean (010) planes in the two grains. Note the new set of perpendicular dislocations introduced into the boundary. From [25].

The new dislocations increase the energy of the boundary sharply as Φ increases from zero because they are far apart. Shockley and Read [26] showed that the energy of this boundary has the same form as the symmetrical tilt boundary with an additional dependence on Φ and that a sharp cusp exists when $\Phi = 0$.

Twist Grain Boundary A more drastic change in the grain boundary structure is produced by rotating the tilt boundary in Figure 13.3 through 90° about an axis in the plane of the boundary and normal to the tilt axis. The boundary is then normal to the <100> axis about which the two grains are rotated, and it is called a twist boundary. It consists of a grid of screw dislocations, as shown in Figure 13.10. The screw dislocations are visible as regions of poor matching where there is a shear displacement parallel to the lines of distortion. It can be shown [31] that if a vector is drawn parallel to a [100] direction in the mean lattice between the two grains in a twist boundary, such as Figure 13.10, the number of [010] screw dislocations that it intersects per unit length, is given by the same formula as that for the number of edge dislocations in a tilt boundary in Eq. (13.2), or $1/D = (2 \sin \theta/2)/b$, where b is the magnitude of the Burgers vector of the screw dislocation. Thus, the energy of a twist boundary increases with the angle of twist in the same general way as the energy of a tilt boundary increases with the angle of tilt.

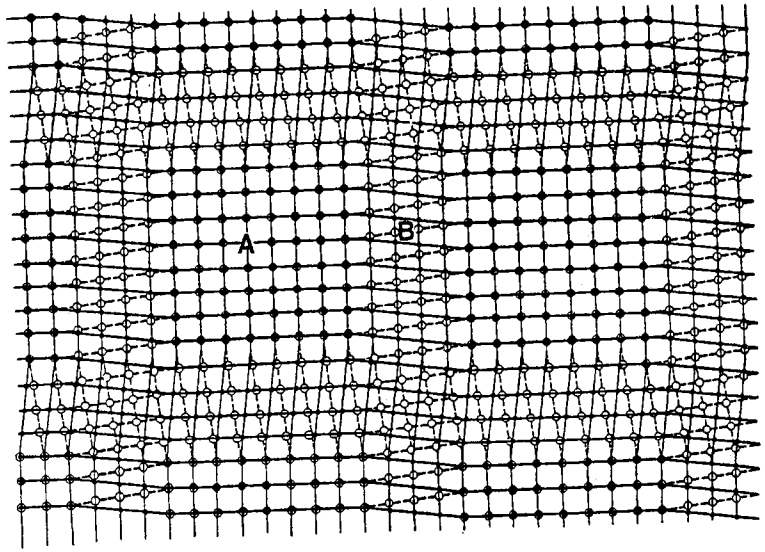

Figure 13.10. A pure (relaxed) twist boundary between two simple cubic crystals. The boundary is in the plane of the figure and the two grains have a small rotation about the cube axis normal to the boundary. The open circles represent atoms just above the plane of the boundary in one grain and the solid circles atoms just below in the opposite grain. Atoms at the interface have been relaxed to produce regions of good atomic matching (*A*) separated by regions of poor matching (*B*), which are the screw dislocations. From [25].

As for tilt boundaries, the energy of a twist boundary should be cusped at angles of twist at which the atoms fit well together in the boundary, although atomistic calculation has shown that these cusps are generally much shallower. For example, the 53° rotation about <100> that produced a cusp in the energy of the cubic tilt boundary, also produces a twist boundary normal to <100> on which the atoms fit uniformly. This is shown in Figure 3.11, where the net of lattice points common to both grains in Figure 3.11 and the similar net of coincident points lying on the corresponding tilt boundary in Figure 13.5, are indicated in each figure. Thus, both boundaries lie on a plane of the coincident atom sites in the two crystals.

Unlike the edge dislocation networks shown in Figures 12.2 and 13.3, it is not possible to reveal the atomic structure of screw dislocation networks by HRTEM, because their Burgers vector lies parallel to the line direction of the dislocations. That is, there is no displacement of the atomic columns perpendicular to the viewing direction when the boundary is edge-on. However, these dislocations can be observed by diffraction contrast imaging techniques in the TEM [32,33] (as can edge or mixed dislocations). Figure 13.12a shows a bright-field TEM image of the dislocation structure in a (001) pure twist low-angle boundary in gold [33,34]. The interface is oriented normal to the viewing direction, and the dislocations are visible as

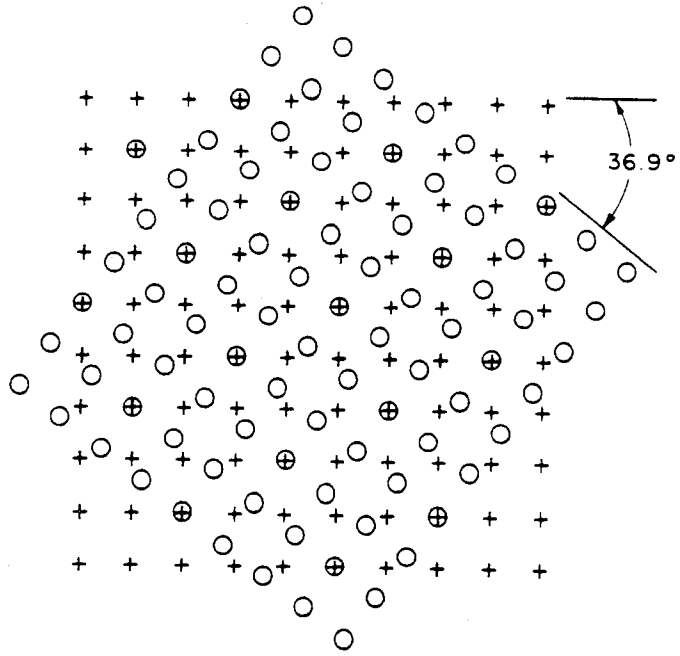

Figure 13.11. Twist boundary of good fit in a simple cubic lattice. The boundary is parallel to the plane of the figure. One lattice is indicated by circles and the other by crosses so that the coincident positions are easily visible. From [27].

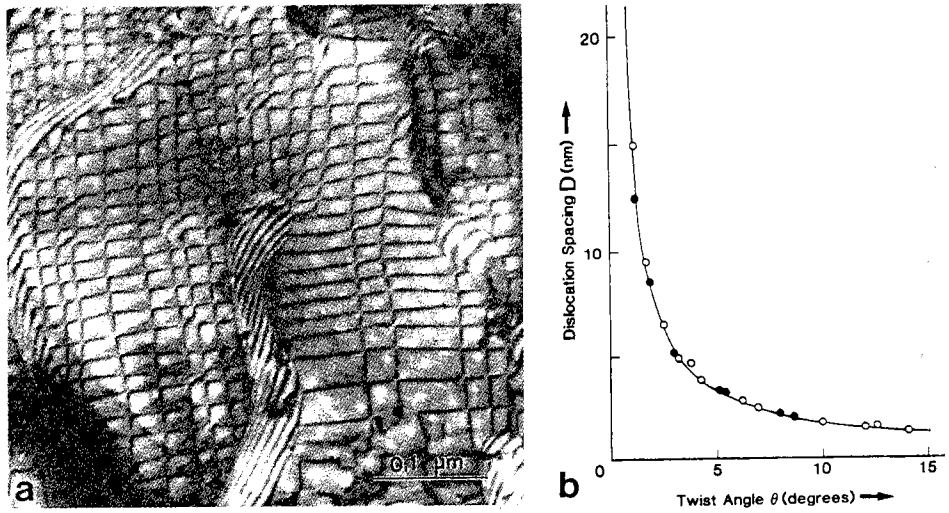

Figure 13.12. (a) Bright field TEM image of a cross-grid of screw dislocations in a pure twist boundary (θ = 1°) in gold. From [34] copyright Taylor & Francis Ltd. (b) Comparison of experimental and calculated spacings of dislocations for (001) twist boundaries in gold. From [33]. The filled circles are the results of Schober and Balluffi [34] and the open circles are from the results of Tan et al. [35].

dark lines in the interface. The boundary consists of an orthogonal array of screw dislocations in agreement with the model shown in Figure 13.10. In their investigation, Schober and Balluffi [34] examined a series of such twist boundaries with misorientations of 1 to 9 degrees and used contrast analyses to establish that the two sets of dislocations in the boundary had Burgers vectors $\mathbf{b} = 1/2[110]$ and $1/2[1\bar{1}0]$. Their results showed that the screw dislocation spacing in the grain boundary varied with θ as expected from the simple relation $D = b/\theta$, as illustrated in Figure 13.12b. The same type of data were also generated for low-angle tilt boundaries and found to agree with the predictions of Eq. (13.2).

Degrees of Freedom of a General Grain Boundary The symmetrical tilt boundary in Figure 13.3 is a special type of boundary, which can be specified by the axis of tilt and the single angle θ. A general grain boundary has five degrees of freedom (DOF), or five quantities that are required to define it. These are often referred to as the five macroscopic degrees of freedom of a general grain boundary. Three values are required to specify the rotation that brings the lattice of one grain parallel to the other and two more values are required to specify the orientation of the boundary plane with respect to one of the grains. These features are illustrated in Figure 13.13. In this figure, we imagine that we cut a crystal along two arbitrary planes, take out the wedge-shaped material in between the two cuts, and bring the two grains together with a twist. The resulting boundary has five degrees of free-

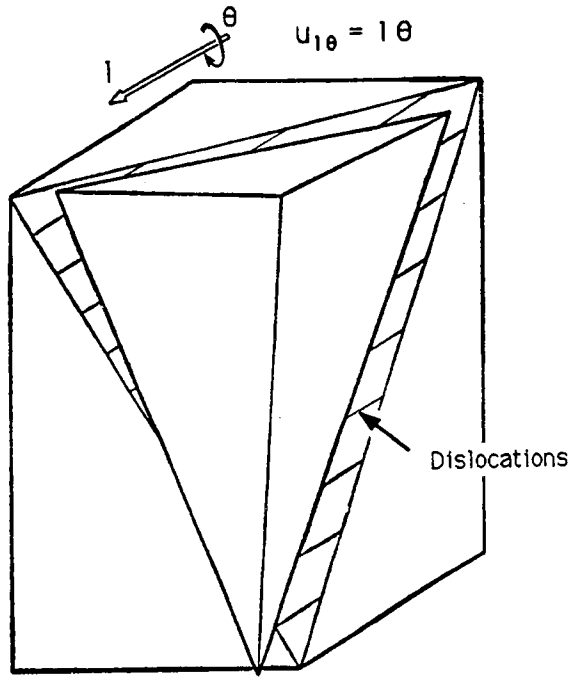

Figure 13.13. Formation of a general grain boundary with five degrees of freedom. In this figure, the misorientation is specified by a rotation θ about a common axis **l** in both grains. In a pure tilt boundary, **l** lies in the plane of the boundary and leads to a set of parallel edge dislocations, indicated by lines on the exposed crystal surface. The vector **l** is normal to the boundary plane in a pure twist boundary. From [25].

dom. If **l** is taken as a unit vector parallel to the axis of relative rotation of the two grains, the rotation between the two grains can be represented by the vector

$$\mathbf{u}_{l\theta} = l\theta, \tag{13.5}$$

which has three independent components or DOF. The orientation of the boundary may then be specified by a unit vector **n** normal to the boundary plane, which requires two additional DOF. A pure twist boundary is thus defined as one where **l** is parallel to **n** and for a pure tilt boundary **l** is perpendicular **n**. The quantity $l\theta$ is often called the axis-angle pair for the grain boundary.

There are various ways of expressing the crystallography of a grain boundary using the five degrees of freedom [2]. One method, which is similar to Figure 13.13 but emphasizes the importance of the interface plane relative to the two grains is illustrated in Figure 13.14. In this figure, we create a general grain boundary by a twist rotation θ about the common grain-boundary plane normal **n**, which is parallel

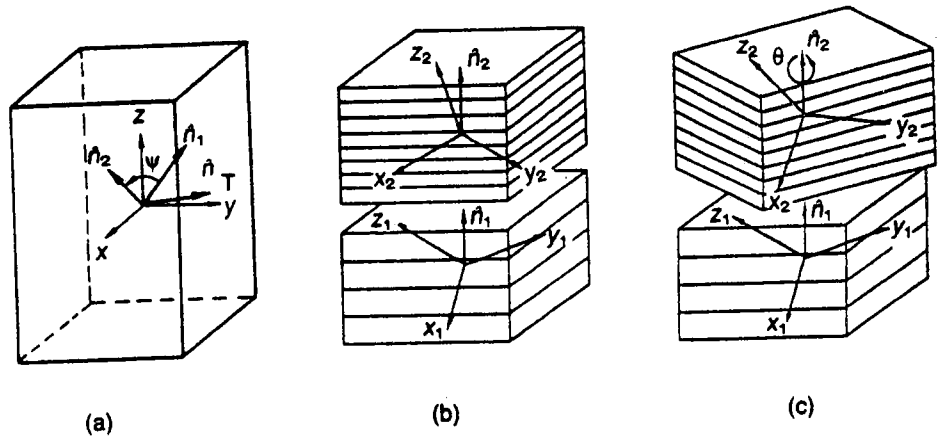

(a) (b) (c)

Figure 13.14. Illustration of the five macroscopic degrees of freedom of an arbitrary bicrystal interface using the interface-plane scheme. (a) The orientations of $\mathbf{n}_1$, $\mathbf{n}_2$ and $\mathbf{n}_T$ in a fixed (*x*,*y*,*z*) coordinate system, (b) a tilt rotation of the two crystal coordinate systems so that $\mathbf{n}_1$ is parallel to $\mathbf{n}_2$, and (c) introduction of the twist component by rotating the top crystal about **n** by the angle θ. From [2].

to the surface normals, $\mathbf{n}_1$ and $\mathbf{n}_2$, of the two grains that form the grain boundary. The degrees of freedom (DOF) of the grain boundary can then be specified as

$$\text{DOF} = \{\mathbf{n}_1, \mathbf{n}_2, \theta\} \tag{13.6a}$$

or in cubic crystals, where it is possible to use the Miller indices of the crystal planes instead of their normals, Eq. (13.6a) is conveniently expressed as

$$\text{DOF} = \{(hkl)_1, (hkl)_2, \theta\}. \tag{13.6b}$$

The twist component ($\mathbf{n}_1$, θ) of a general grain boundary described by Eq. (13.6a) is governed by θ and the grain boundary normal **n**, whereas its tilt component ($\mathbf{n}_T$,ψ), governed by the condition that $\mathbf{n}_T$ is perpendicular to $\mathbf{n}_1$,$\mathbf{n}_2$, is given by

$$\mathbf{n}_T = \frac{[\mathbf{n}_1 \times \mathbf{n}_2]}{\sin\psi} \tag{13.7a}$$

and

$$\sin\psi = |\mathbf{n}_1 \times \mathbf{n}_2|, \tag{13.7b}$$

where $\mathbf{n}_T$ is a unit vector defining the orientation of the tilt axis and ψ denotes the tilt angle, as illustrated in Figure 13.14. Using this method, referred to as the interface-plane scheme [2], $\psi = 0$ for a pure twist boundary with twist angle θ, and $\theta = 0$

for a pure tilt boundary with tilt angle ψ. A general grain boundary thus has values for both θ and ψ.

The interface-plane scheme developed for grain boundaries is similar to the notation that is often used to describe the interface plane or orientation relationship between two different phases at a heterophase interface. In the case of two different phases α and β, the interface is often specified by a set of parallel (hkl) planes and $[uvw]$ directions in the two phases as

$$(hkl)_\alpha \| (hkl)_\beta;\ [uvw]_\alpha \| [uvw]_\beta, \tag{13.8}$$

where the symbol $\|$ is used to indicate the parallel relationship and the $[uvw]$ directions are contained in the parallel (hkl) planes [36]. Specifying a set of parallel directions within the (hkl) planes is similar to specifying a rotation angle θ, as in Eq. (13.6a). It is often found that heterophase interfaces do not lie along the parallel set of planes in the two phases given by Eq. (13.8). In this case, it is common to specify the orientation relationship between the two phases according to Eq. (13.8) and then to denote the interface plane as an (hkl) plane in either (or both) of the phases. For the situation of precipitates in a matrix, the matrix plane is often chosen. An example of such notation is shown by the $(474)_\gamma$ interface in Figure 12.7, and additional examples are discussed in Section 14.6.1.

In addition to the five macroscopic degrees of freedom, there are three independent translational (or so-called microscopic) degrees of freedom for a grain boundary involving translations $\mathbf{T} = (T_x, T_y, T_z)$ parallel (x, y) and perpendicular (z) to the interface plane. Computer simulations and HRTEM have shown that such translations occur frequently at grain boundaries. From a thermodynamic viewpoint the z component of $\mathbf{T}$ perpendicular to the interface is important, because it accounts for any volume expansion in the interface. Such an excess free volume at the interface is expected to be closely related to its excess free energy and to give rise to stresses near the interface that are similar to the well-known surface stress discussed with regard to surfaces in Part II. This so-called excess free volume per unit area of the interface [2] is defined by

$$\Delta V_i = (\partial V/\partial A)_{T,P,N_i}, \tag{13.9}$$

where the volume expansion is given in units of the lattice parameter. We see in a later section on atomistic modeling of grain boundaries that this volume expansion is an important parameter related to the grain boundary energy.

Frank's Formula for the Dislocation Content of a Boundary The dislocation content of a general grain boundary can be determined according to the theory of Frank [37]. The same procedure can be applied to heterophase interfaces where there is a change in crystal structure across the interface [1,38]. This theory is illustrated for a grain boundary geometrically in Figure 13.15. In Figure 13.15a, a reference lattice has been cut along AA' by a plane with a normal specified by the

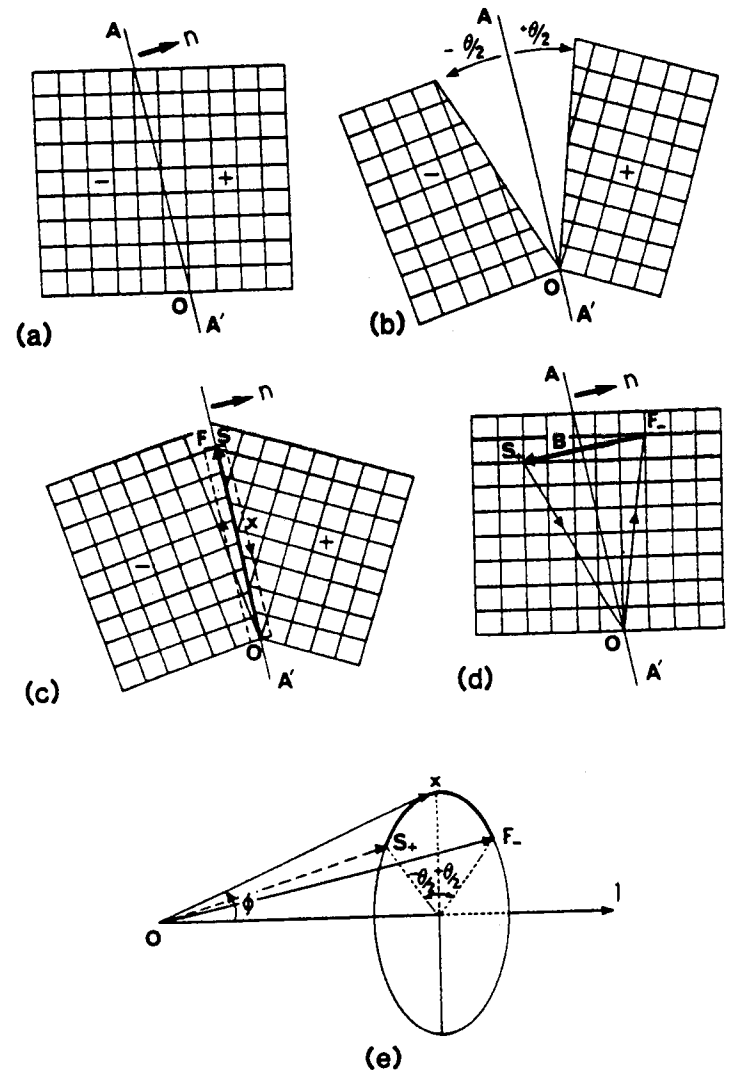

Figure 13.15. Illustration of the derivation of the net Burgers vector **B** crossing a vector **x** in a planar grain boundary AA' with unit normal **n**, where lattice + is rotated with respect to lattice − by an angle θ in a right-handed sense about an axis **l** directed into the plane of the page through the point O. From [33].

unit vector **n**, so as to divide the lattice into two crystals represented by + and –. In Figure 13.15b, crystal + is rotated by an angle $+\theta/2$ and crystal – by an angle of $-\theta/2$ in a right-handed sense about an axis defined by a unit vector **l** passing through the lattice point *O* and directed into the page. In Figure 13.15c, these two misoriented lattices are extended until they join at the original cut, forming a grain boundary. A vector **x**, which can have any direction in this boundary plane, is then chosen to extend from the origin *O* over several unit cells, as illustrated in Figure 13.15c. The net Burgers vector of the dislocations in the grain boundary which intersects **x** can be determined by comparing a Burgers circuit containing the vector **x** in the bicrystal with an equivalent circuit in the reference lattice. This is done using the finish-to-start, right-hand (FS/RH) convention [25,39] with the closure failure being made in the good crystal. The circuit in the bicrystal (Fig. 13.15c) is a closed circuit made in a right-handed sense around an axis parallel to $(\mathbf{x} \times \mathbf{n})$, where **n** is defined as pointing from crystal – into crystal +. This circuit is also made in a right-handed sense with respect to the rotation axis **l**. The circuit starts at *S*, the end-point of the vector **x** extends through crystal + to the origin *O* and then returns through crystal – to the point *F*, which is coincident with *S*. In the reference lattice redrawn in Figure 13.15d, the first part of the circuit *SO* in the crystal + is represented by S_+O and the second part of the circuit, *OF* in crystal –, is represented by OF_-. There is clearly a closure failure $F_-S_+ = \mathbf{B}$ in the reference lattice, and this defines the net Burgers vector of those dislocations contained in the boundary that are intersected by the vector **x**. In general, the vector **x** makes an angle Φ with **l** as shown in Figure 13.15e, so the resulting vector **B** has a magnitude given by

$$|\mathbf{B}| = |\mathbf{x}| 2 \sin(\theta/2) \sin \Phi \tag{13.10}$$

with a direction along $(\mathbf{x} \times \mathbf{l})$. Furthermore, because

$$|\mathbf{x} \times \mathbf{l}| = |\mathbf{x}| \sin \Phi, \tag{13.11}$$

then

$$\mathbf{B} = (\mathbf{x} \times \mathbf{l}) 2 \sin(\theta/2), \tag{13.12a}$$

which, for small θ, yields

$$\mathbf{B} = (\mathbf{x} \times \mathbf{l})\theta. \tag{13.12b}$$

Equation (13.12b) is the general formula derived by Frank for the net Burgers vector of the dislocations required geometrically to accommodate the misorientation at a general grain boundary. The quantity **B** is the sum of the Burgers vectors of all the dislocations intersected by **x** or

$$\mathbf{B} = \sum_i n_i \mathbf{b}_i, \tag{13.13}$$

where n_i is the number of dislocations of Burgers vectors $\mathbf{b}_i$ cut by **x**. When the net Burgers vector **B** of Eq. (13.12) arises from three independent arrays of grain boundary dislocations with noncoplanar Burgers vectors $\mathbf{b}_1$, $\mathbf{b}_2$ and $\mathbf{b}_3$, with line directions parallel to unit vectors $\boldsymbol{\xi}_1$, $\boldsymbol{\xi}_2$ and $\boldsymbol{\xi}_3$ and with spacings D_1, D_2 and D_3, then Eq. (13.12) can be written as

$$n_1\mathbf{b}_1 + n_2\mathbf{b}_2 + n_3\mathbf{b}_3 = 2 \sin(\theta/2)(\mathbf{x} \times \mathbf{l}), \tag{13.14}$$

where the values of n_i with their appropriate signs are given by $n_i = \mathbf{N}_i \cdot \mathbf{x}$, where $\mathbf{N}_i$ is a vector in the plane of the boundary normal to the line directions of the dislocations in the *i*th array, with a magnitude equal to the reciprocal of their spacing. It is thus defined as

$$\mathbf{N}_i = \frac{\mathbf{n} \times \boldsymbol{\xi}_i}{D_i}. \tag{13.15}$$

Several points should be made regarding Eqs. (13.12) and (13.14). Firstly, they apply only to boundaries that are essentially flat and have no long-range stress field (i.e., the elastic distortion is restricted to the region close to the dislocations). Secondly, the equations do not uniquely determine the dislocations present at the boundary or their pattern for a given crystal and boundary. Thus, a variety of possible dislocation structures could exist and the most probable one is the one with the lowest energy. Thirdly, the density of a given set of dislocations in a boundary is directly proportional to θ for small θ. Fourthly, each set of dislocations is straight, equally spaced and parallel even for a boundary containing several sets of dislocations with different Burgers vectors. Lastly, a general boundary requires three sets of dislocations with three non-coplanar Burgers vectors at the boundary, and Frank's formula can be applied to analyze all possible cases, either to determine the possible dislocations arrangements if **n**, **l** and θ are known, or conversely, to find the orientation, and so on, if the dislocation content is specified. These cases are analyzed elsewhere [25,33] and are not discussed further here.

13.2.2. O-Lattice Formulation

The Read and Shockley dislocation model for low-angle tilt and twist grain boundaries discussed in Section 13.2.1 is appealing because it is relatively easy to understand both physically and analytically and because it has been shown to be experimentally correct for low-angle grain boundaries. Unfortunately, the dislocation model becomes unphysical for high tilt angles, and an alternative description for the structure and energy of high-angle grain boundaries is required. Although several different approaches to this problem have been tried, none has the sort of predictive capability and accuracy that is usually desired. In fact, it is only recently that extensive atomistic simulations have provided sufficient data to explain the properties of high-angle grain boundaries in a simple physical manner [2,7].

The purpose of this book is to explain the structure and properties of inter-

faces using relatively simple analytical treatments that are based on a nearest-neighbor atomistic model of the interfaces whenever possible. In keeping with this theme, we defer discussion of the atomistic calculations of grain boundary structure and energies until we have considered two methods for quantifying interfacial structure that have gained popularity and that relate to the previous dislocation description of interfacial structure. These are the so-called O-lattice and coincident site lattice/displacement shift complete (CSL/DSC) descriptions of grain and interphase boundary structure. Both treatments are geometrical models based on the matching of hard-sphere atoms across an interface and they complement the previous hard-sphere models used to understand solid–vapor and solid–liquid interfaces in Parts II and III. These theories build on the Read and Shockley dislocation model and Frank's equation for the dislocation content of a grain boundary; we examine them in some detail prior to the atomistic simulations. The O-lattice and CSL/DSC theories are developed for grain boundaries for simplicity, but examples are provided to demonstrate that they can be applied directly to heterophase interfaces.

Bollmann developed a technique for analyzing the structure of grain and interphase interfaces that is quite general and has a number of useful properties [40–43]. His method is based on the concept of the O-lattice, which describes the matching and mismatching of oriented lattices at an interface. We develop this theory by reference to Frank's formula for the Burgers vector content of a general grain boundary in Figure 13.15 and show that in fact, Bollmann's O-lattice equation is mathematically similar to Frank's formula in Eq. (13.12).

If we refer to Figure 13.15d, the net Burgers vector **B** of the dislocations in the boundary that are intersected by the vector **x** is given by

$$\mathbf{B} = F_- S_+ = OS_+ - OF_-.$$

If $\mathbf{R}_+$ is defined as the rotation tensor $(\mathbf{l}, +\theta/2)$ which transforms the reference lattice into +, and $\mathbf{R}_-$ as the rotation tensor $(\mathbf{l}, -\theta/2)$ which transforms the reference lattice into lattice –, then

$$OS_+ = \mathbf{R}_+^{-1}\mathbf{x} \quad \text{and} \quad OF_- = \mathbf{R}_-^{-1}\mathbf{x},$$

so that

$$\mathbf{B} = (\mathbf{R}_+^{-1} - \mathbf{R}_-^{-1})\mathbf{x}. \tag{13.16}$$

In Eq. (13.16), **B** and **x** are expressed with respect to the reference lattices in Figures 13.15a and d. However, if one of the lattices is chosen as the reference lattice, say crystal +, and **B** and **x** are expressed in this lattice, then Eq. (13.16) becomes

$$\mathbf{B} = (\mathbf{I} - \mathbf{R}^{-1})\mathbf{x}, \tag{13.17}$$

where **R** is the rotation tensor that transforms lattice + into lattice –, and **I** is the identity matrix.

The advantage of expressing the relationship between the two crystals by Eq. (13.17) is that it can be readily generalized to apply to heterophase interfaces by replacing the rotation tensor **R** with a general deformation tensor **A**, which transforms the lattice of crystal + into the lattice of crystal –, and involves a strain as well as a rotation [1,38,44]. Thus, with respect to crystal +, the net Burgers vector of those dislocations contained in the heterophase interface that are intersected by a vector **x** is given by

$$\mathbf{B} = (\mathbf{I} - \mathbf{A}^{-1})\mathbf{x}. \tag{13.18}$$

The properties of Eq. (13.18) are similar to those for the grain boundary described in Eqs. (13.12) and (13.14) in that for a general heterophase interface, **B** must be the resultant Burgers vector of at least three independent arrays of interfacial dislocations with non-coplanar Burgers vectors. Thus, we can write an equation similar to Eq. (13.14) but for the case of two different crystal lattices,

$$n_1\mathbf{b}_1 + n_2\mathbf{b}_2 + n_3\mathbf{b}_3 = (\mathbf{I} - \mathbf{A}^{-1})\mathbf{x}, \tag{13.19}$$

where in this case **n** is the unit vector normal to the heterophase interface and is directed from crystal – into crystal +. The similarity between Eqs. (13.19) and (13.14) indicates that the arrays of dislocations in heterophase interfaces can be considered in the same way as for grain boundaries.

We are now able to derive the basic equation of O-lattice theory after having expressed Eq. (13.18) in a way that is applicable to any type of interface through a matrix **A**, which relates the two crystal lattices. If two misoriented crystal lattices, specified here as 1 and 2 to indicate that they may be different lattice types, are allowed to interpenetrate, there will be a periodic set of points in space (not generally lattice points of either lattice), where, for each point, the internal coordinates in a cell of lattice 1 are identical with the internal coordinates in a cell of lattice 2. This set of points defines Bollmann's O-lattice [40]. In terms of a general deformation tensor **A**, which transforms lattice 1 into lattice 2, a point defined by a vector $\mathbf{x}^{(2)}$ in lattice 2 is generated from a point defined by a vector $\mathbf{x}^{(1)}$ in lattice 1 according to

$$\mathbf{x}^{(2)} = \mathbf{A}\mathbf{x}^{(1)}. \tag{13.20}$$

A point on the O-lattice is therefore defined by a vector $\mathbf{x}^{(O)}$ when $\mathbf{x}^{(2)}$ differs from $\mathbf{x}^{(1)}$ by a translation vector $\mathbf{b}^{(L)}$ of lattice 1, that is, when

$$\mathbf{x}^{(2)} = \mathbf{x}^{(O)} = \mathbf{x}^{(1)} + \mathbf{b}^{(L)} = \mathbf{A}\mathbf{x}^{(1)}. \tag{13.21}$$

From this set of equations, we have

$$\mathbf{b}^{(L)} = (\mathbf{I} - \mathbf{A}^{-1})\mathbf{x}^{(O)}, \tag{13.22}$$

which is the basic equation of O-lattice theory [40]. This equation gives the O-lattice vectors in terms of the vectors of crystal lattice 1. In this equation, $\mathbf{b}^{(L)}$ corre-

sponds to **B** in Eqs. (13.12) or (13.18) and $\mathbf{x}^{(O)}$ corresponds to **x**. Thus, the vectors $\mathbf{x}^{(O)}$ cross dislocations with Burgers vectors summing to $\mathbf{b}^{(L)}$, referred to lattice 1.

As an example, we will derive the O-lattice solution for two simple cubic crystal lattices that are rotated about the [001] axis referring to the coordinate system of lattice 1, as illustrated in Figure 13.16. This example follows the work of Smith and Pond [42]. The transformation tensor **A** is a rotation **R**, which can be written

$$\mathbf{A} = \mathbf{R} = \begin{bmatrix} \cos\theta & -\sin\theta & 0 \\ \sin\theta & \cos\theta & 0 \\ 0 & 0 & 1 \end{bmatrix},$$

so that

$$\mathbf{A}^{-1} = \begin{bmatrix} \cos\theta & \sin\theta & 0 \\ -\sin\theta & \cos\theta & 0 \\ 0 & 0 & 1 \end{bmatrix}$$

and

$$(\mathbf{I} - \mathbf{A}^{-1}) = \begin{bmatrix} 1-\cos\theta & -\sin\theta & 0 \\ \sin\theta & 1-\cos\theta & 0 \\ 0 & 0 & 0 \end{bmatrix}.$$

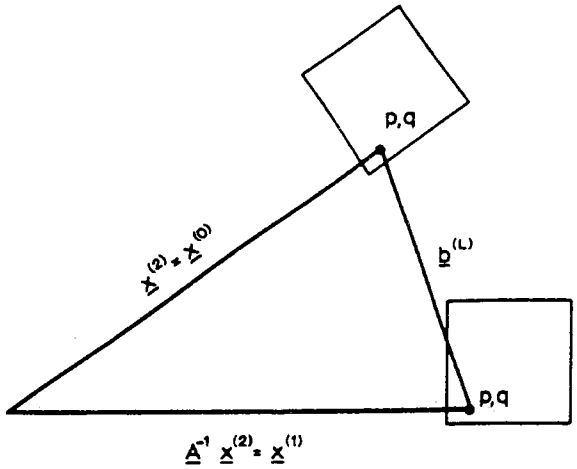

Figure 13.16. Diagram showing the difference vector $\mathbf{b}^{(L)}$ between $\mathbf{x}^{(1)}$ and $\mathbf{x}^{(2)}$ for a simple cubic unit cell having an O-point with internal coordinates (*p*,*q*). From [42].

Substituting $(\mathbf{I} - \mathbf{A}^{-1})$ into Eq. (13.22) gives

$$\begin{bmatrix} 1-\cos\theta & -\sin\theta & 0 \\ \sin\theta & 1-\cos\theta & 0 \\ 0 & 0 & 0 \end{bmatrix} \begin{bmatrix} x_1 \\ x_2 \\ x_3 \end{bmatrix} = \begin{bmatrix} b_1 \\ b_2 \\ b_3 \end{bmatrix},$$

where x_1, x_2 and x_3 and b_1, b_2 and b_3 are the components of $\mathbf{x}^{(O)}$ and $\mathbf{b}^{(L)}$. This expression can be written explicitly as three linear equations:

$$(1-\cos\theta)x_1 - (\sin\theta)x_2 + 0x_3 = b_1 \tag{13.23a}$$

$$(\sin\theta)x_1 + (1-\cos\theta)x_2 + 0x_3 = b_2 \tag{13.23b}$$

$$0x_1 + 0x_2 + 0x_3 = b_3, \tag{13.23c}$$

where $b_3 = 0$ and x_3 can have any value. Equation (13.23c) means that there are no uncancelled components of the Burgers vector parallel to the rotation axis of the grain boundary x_3. Therefore, the O-lattice consists of lines going through points $\mathbf{x}_1^{(O)}$ and $\mathbf{x}_2^{(O)}$, which have discrete values. The primitive vectors of the O-lattice in the plane perpendicular to the rotation axis (i.e., for a pure twist boundary) can be found by assuming a Burgers vector of unity and solving Eqs. (13.23a) and (13.23b) simultaneously as

$$\begin{bmatrix} 1-\cos\theta & -\sin\theta \\ \sin\theta & 1-\cos\theta \end{bmatrix} \begin{bmatrix} x_1 \\ x_2 \end{bmatrix} = \begin{bmatrix} b_1 \\ b_2 \end{bmatrix},$$

so

$$\mathbf{x}_{1,2}^{(O)} = \begin{bmatrix} x_1 \\ x_2 \end{bmatrix} = \begin{bmatrix} 1/2 & 1/2\cot(\theta/2) & 1 \\ -1/2\cot(\theta/2) & 1/2 & 0 \end{bmatrix},$$

and the primitive vectors are

$$\mathbf{x}_1^{(O)} = 1/2, -1/2\cot(\theta/2) \tag{13.24a}$$

$$\mathbf{x}_2^{(O)} = 1/2\cot(\theta/2), 1/2. \tag{13.24b}$$

Note that $\mathbf{x}_1^{(O)}$ and $\mathbf{x}_2^{(O)}$ are continuous functions of θ and that, when θ is small, Eqs. (13.24) reduce to the result given by Frank's formula in Eqs. (13.2) and (13.12); that is, the dislocation spacing D is given by b (unity in this case) divided by θ. Also notice that there are particular values where the cot $(\theta/2)$ in Eqs. (13.24) are rational, for example, when cot $(\theta/2)$ = integer. This situation was illustrated previously in Figure 13.5 where cot $(\theta/2) = 14$. Whenever the cot $(\theta/2) = 2n$ for both $\mathbf{x}_1^{(O)}$ and $\mathbf{x}_2^{(O)}$ (i.e., it is even for both), the O-point has integral coordinates and is thus a crystal lattice site. When either or both of the O-points are odd, the O-point is

either in the center of an edge or in the center of a crystal cell. This illustrates the general result that points of the O-lattice need not coincide with crystal lattice sites.

In the derivation of Eq. (13.22), it was assumed that the points defined by the vectors $\mathbf{x}^{(O)}$ have identical internal coordinates in both lattices 1 and 2, and the $\mathbf{b}^{(L)}$ vectors are all lattice translation vectors. Physically, this means that the interface under consideration is comprised of perfect crystal dislocations. In the section that follows, we see that other dislocations with Burgers vectors that are less than a full lattice translation are possible at an interface. This does not mean that the O-lattice theory is incorrect but rather, that the choice of Burgers vectors at an interface is ambiguous and some additional criteria must be considered to determine the most favorable Burgers vectors at the interface. This is a weakness of the O-lattice theory in terms of its predictive capabilities. Another shortcoming is that the theory can be used to analyze an interface if **A** and **n** and/or the dislocation Burgers vectors $\mathbf{b}^{(L)}$ are known, but it cannot be used to predict **n** or $\mathbf{b}^{(L)}$ without knowing **A** and using some other criteria.

The physical interpretation of the O-lattice in terms of grain boundaries is that the O-points in Eq. (13.22) are points of geometric registry (minimum strain) between crystal lattices 1 and 2. Between each of these O-points, there is an accumulating disregistry that reaches the value $\mathbf{b}^{(L)}$ at a neighboring O-point. Thus, it is imagined that the misfit between any set of O-points is concentrated onto planes between the O-points just as the misfit between two identical but slightly rotated lattices relaxes into a low-angle boundary network of dislocations, as in Figure 13.10. In the example above, where the axis of rotation was parallel to [001] in the two lattices, the O-lattice construction yields O-lines parallel to the rotation axis with two orthogonal planes of dislocations bisecting the space between the O-lines as illustrated in Figure 13.17. Note that a plane taken perpendicular to the O-lines in this figure would look exactly like Figure 13.10. In the case of a general grain or interphase boundary, the set of planes on which misfit is condensed defines a three-dimensional cell structure with each cell enclosing an O-point. Consequently, wherever the interface plane cuts a cell wall there is a dislocation with Burgers vector $\mathbf{b}^{(L)}$.

Although this section is primarily concerned with the structure of grain boundaries and therefore a rotation **R** between two crystals, it is convenient to illustrate the use of the O-lattice theory for a different kind of transformation tensor **A**, in which there is a simple dilatation Δa between two simple cubic crystal lattices. This also serves to emphasize the generality of the O-lattice formulation to other types of transformations. We see a second example of the O-lattice applied to a rotation between two crystals in the next section. The dot patterns included as Appendix D can be used to duplicate these and other examples.

Figure 13.18a shows schematically, a (001) projection of the O-lattice between two simple cubic lattices with the same orientation but different lattice parameters, where crystals 1 and 2 are represented by dots and crosses, respectively, and the O-points are circled. The two lattices are related by a simple dilatation Δa and inspection shows that the O-lattice itself is a simple cubic lattice. The $\mathbf{b}^{(L)}$ vectors lie between the O-points, that are indicated by circles in the figures. The dislocation spacing in the O-lattice is given as $(1 + \Delta a)/\Delta a$, which is equivalent to the inverse

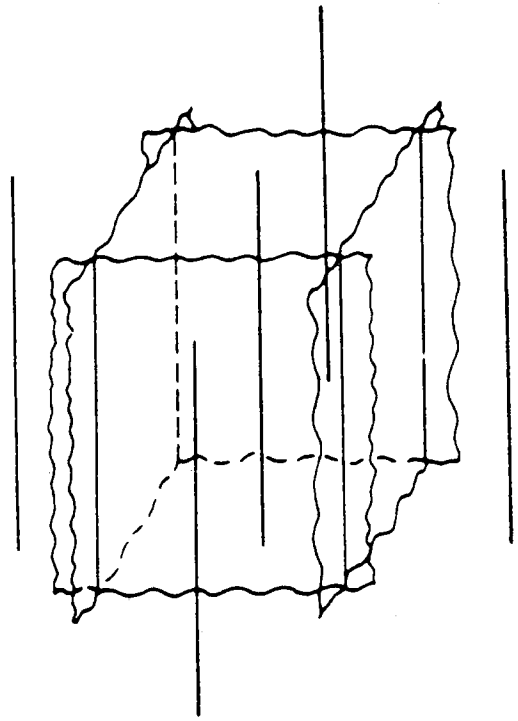

Figure 13.17. Schematic representation of the O-lines and dislocation cell walls associated with the O-lattice of two simple cubic lattices rotated about a common [001] axis. From [42].

of the misfit δ in Eq. (13.18). Figure 13.18b shows the planes that bisect the O-lattice vectors perpendicular to the plane of the figure. These form square cell walls around the O-lattice points in three dimensions. In Figure 13.18c an interface path is chosen so that it passes through as many O-points as possible in order to maximize the amount of good matching in the interface. When crystal 1 is removed from above the interface plane in Figure 13.18c and crystal 2 is removed from the interface plane downward, the interface in Figure 13.18d results. In this interface, the O-points are regions of good matching and these are separated by regions where relaxation of the interface into dislocations has occurred (where the cell walls were crossed). This illustrates the O-lattice construction, which can be performed analytically using the basic O-lattice equation (Eq. 13.22).

13.2.3. Coincident Site and Displacement Shift Complete Lattices

The previous O-lattice theory provides us with a convenient mathematical technique for analyzing possible dislocation structures between two arbitrary lattices in space when their orientation relationship is known. It is a useful technique, but it

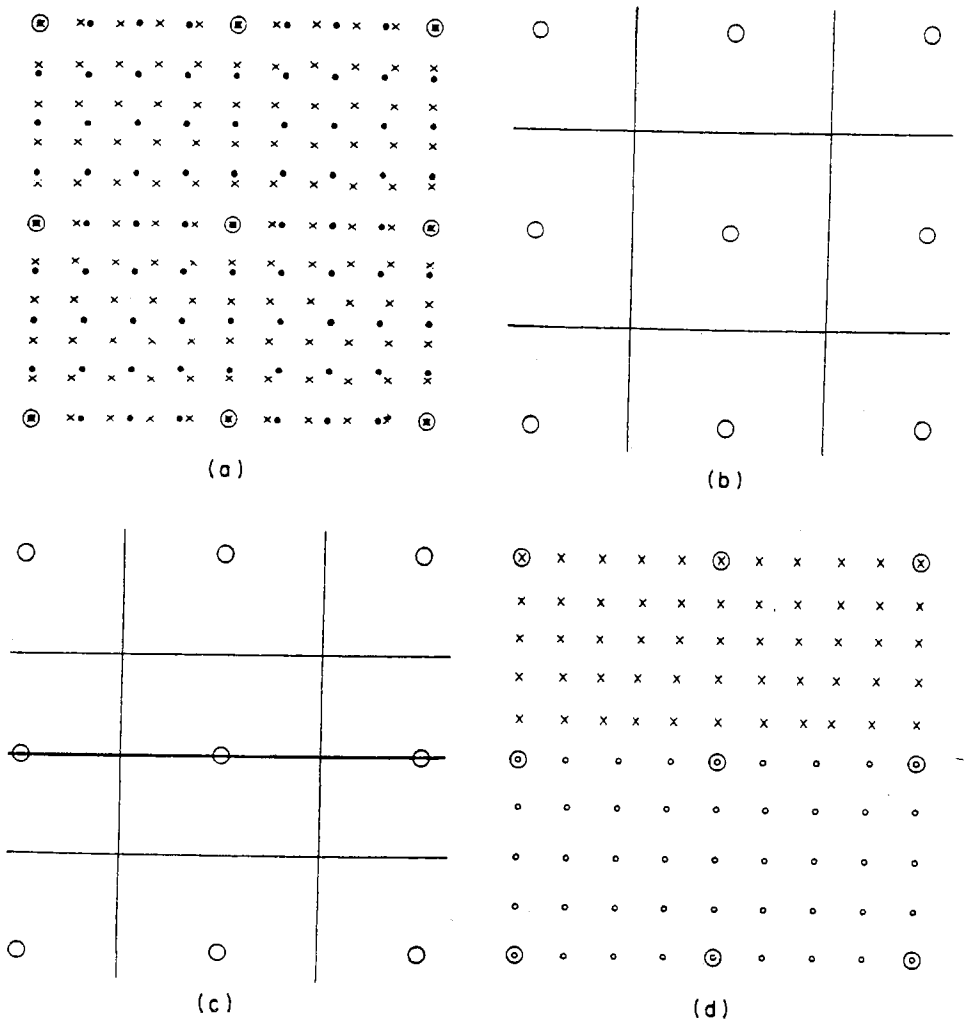

Figure 13.18. Illustration of the O-lattice construction for a dilatation between two simple cubic lattices: (a) (001) projection of the O-lattice, (b) cells walls drawn midway between the O-points, (c) interface path through highest density of O-points, and (d) section showing dislocations at the interface. From [42].

has limitations in that it cannot predict certain aspects of interfacial structure that are commonly found at interfaces, such as ledges and partial dislocation structures. In addition, as with the Read and Shockley analysis, its meaning becomes unclear in the case of high-angle grain boundaries. An alternate technique for quantifying the interfacial structure of grain and interphase boundaries for any angle of tilt or orientation is provided by the coincident site lattice (CSL) and displacement shift complete (DSC) lattice constructions provided in this section. The CSL/DSC theory was actually developed before O-lattice theory, but the O-lattice was introduced first in this chapter because of its close relation to Frank's equation for the dislocation content of a grain boundary in Section 13.2.1. In this section, we develop the CSL/DSC construction for grain boundaries using a pure tilt boundary for purposes of illustration, and then show that the CSL/DSC framework can be readily extended to include heterophase interfaces as well.

Coincident Site Lattice We have seen previously in Figures 13.5 and 13.11 that when two identical interpenetrating lattices are rotated from initial coincidence around a lattice point, there are certain discrete rotation angles where lattice points other than the origin coincide. An example often found in the literature is shown in Figure 13.19a, in which two simple cubic lattices, one indicated by solid dots and the other by open circles, are outlined by a dashed and solid square, respectively. The two lattices have been rotated 36.9° about an axis perpendicular to the plane of the figure, as in Figure 13.11, and the pattern that results is often referred to as the dichromatic pattern. In this case cot $(\theta/2) = 3$ and the [310] vector in one lattice is coincident with the $[3\bar{1}0]$ vector in the other lattice. This rotation causes one-fifth of the lattice points of the simple cubic crystal to coincide, and this is true for f.c.c. and b.c.c. lattices as well. The coincident points themselves form a lattice, called the coincident site lattice (CSL), which is indicated by filled circles and outlined in Figure 13.19b. The lattice vectors of the CSL are given as

$$1/2[310]_1 \| 1/2[3\bar{1}0]_2,$$

$$1/2[\bar{1}30]_1 \| 1/2[130]_2 \text{ and}$$

$$1/2[12\bar{1}]_1 \| 1/2[21\bar{1}]_2.$$

The CSL is characterized by Σ, the inverse density of coincident sites, alternatively expressed as the ratio of the area of the coincident lattice cell to that of the original lattice. For the example shown in Figure 13.19, $\Sigma = 5$, because two out of every ten atoms (i.e., the corner atoms) in each unit cell of the CSL lattice are coincident. Any rational <*uvw*> lattice vector can be used to generate a CSL; it has been shown [46] that all possible CSLs in the cubic system can be described by the function

$$\Sigma = x^2 + Ny^2, \tag{13.25}$$

where x and y are nonnegative integers representing the Cartesian coordinates of the lattice point joined to the origin, and $N = u^2 + v^2 + w^2$. A CSL is always generated for a rotation of 180° about a rational direction <*uvw*>. When the value of Σ determined from Eq. (13.25) is even, it must be divided by two until an odd number results. For example, a <310> vector where $\Sigma = 10$ and a <210> vector where $\Sigma = 5$ generate the same $\Sigma = 5$ CSL, shown in Figure 13.19b. Thus the $\Sigma = 10$ CSL must

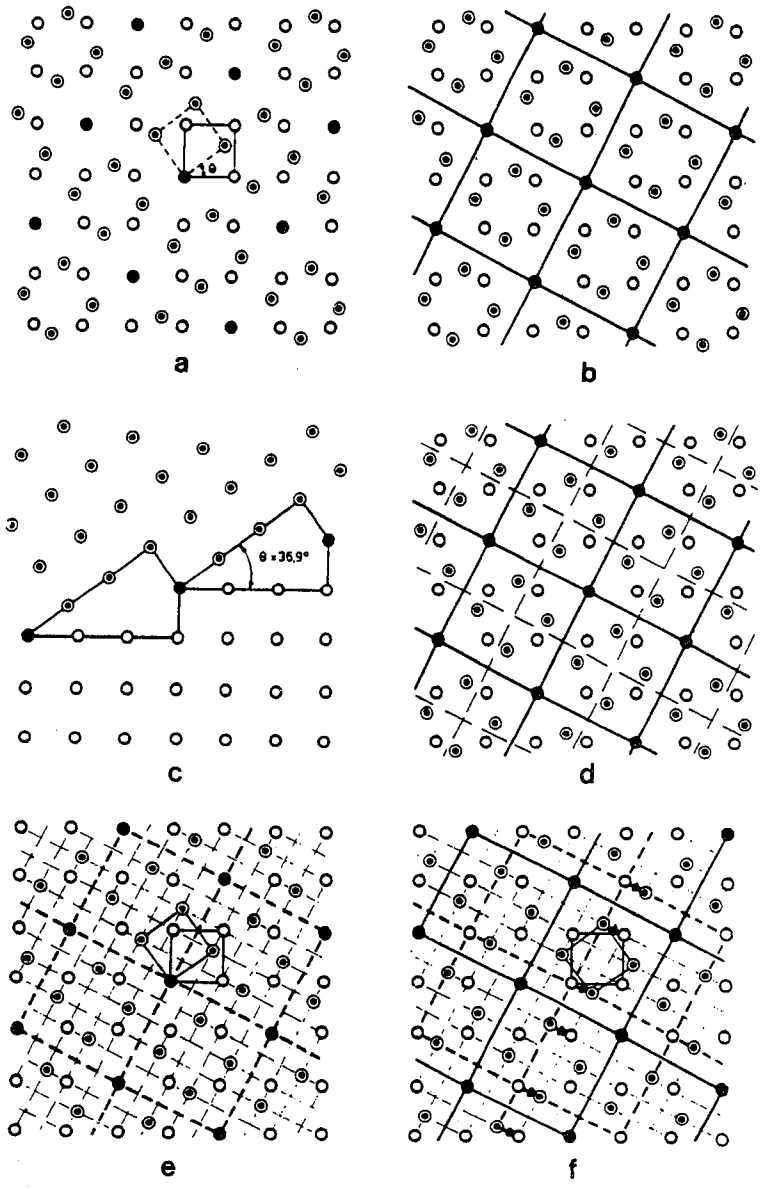

Figure 13.19. (a) Dichromatic pattern produced by rotating two cubic crystals 36.9° about [001]. (b) $\Sigma = 5$ CSL outlined in the dichromatic pattern. (c) A possible $(130)_1$, $(130)_2$ grain boundary generated from the CSL. (d) The O-lattice (= CSL plus the dashed lines). (e) The DSC lattice of the $\Sigma = 5$ dichromatic pattern. (f) The dichromatic pattern after translation by a DSC vector; dashed lines indicate old CSL and solid lines indicate new CSL. From [45].

be divided by two to yield the $\Sigma = 5$ CSL in Figure 13.19b. The angle of misorientation corresponding to a particular CSL is given by

$$\theta = 2 \tan^{-1}(y/x) N^{1/2}, \tag{13.26}$$

where $\theta = 180°$ corresponds to $x = 0, y = 1$. Thus, the rotation of 180° around <*uvw*> in a cubic system gives rise to a CSL of $\Sigma = u^2 + v^2 + w^2$ if N is odd or $N/2$ if N is even.

Because the same values of Σ may be generated by Eq. (13.25) from different sets of x, y and N, different CSLs that yield the same values are distinguished by labeling them a, b, c, and so on. The corresponding axis–angle pairs for coincidence boundaries in the cubic system for Σ values ranging from 1 to 19 calculated from Eq. (13.25) are shown in Table 13.2. Usually, both Σ and the axis–angle pair are specified in CSL nomenclature, that is, $\Sigma = 5$, 36.9°/[001] for Figure 13.19b. The inclination of the boundary is then specified by the Miller indices of the boundary plane in both lattices, that is, $(hkl)_1(hkl)_2$, similar to the DOF specified in Eq. 13.6b). For the symmetric tilt boundary in Figure 13.19c, the complete CSL notation is $\Sigma = 5$ (310) 36.9°/[001], where only one (hkl) is necessary, because the boundary is symmetric. The values of θ in Table 13.2 correspond to ideal coincidence boundaries. A more extended tabulation is given by Mykura [47].

In Figure 13.19c a (310) boundary plane was chosen, and opposite lattice types were discarded from either side of the boundary, leaving a grain boundary composed of typical structural units, as indicated in the figure. Although the density of coincident sites depends only on the orientation relationship between two crystals, the density of coincident sites at a boundary depends on the choice of the boundary plane intersecting the CSL. Special grain boundaries have a high density of coincident sites and therefore a low value of Σ. It seems reasonable to expect that the energy of a grain boundary should be proportional to Σ, but except in the case of some special grain boundaries, it has been shown that there is no simple correlation between the two. This is a disappointment of the CSL theory, but we now know that this lack of correlation is from volume expansions and translations that frequently occur at grain boundaries to minimize the energy of the boundary. Such relaxations cannot be predicted from simple geometric theories.

Figure 13.20 shows an HRTEM image of a $\Sigma = 5$ (310) 36.9°/[001] symmetrical tilt grain boundary in cubic nickel oxide [48]. The atomic columns appear as dark spots in this image and a regular pattern of structural units at the boundary is evident as predicted by the CSL construction in Figure 13.19c. However, note that there is a lack of mirror symmetry across the boundary in the HRTEM image that is present in the unrelaxed CSL model in Figure 13.19c. This is due to a slight translation of the boundary involving the three microscopic degrees of freedom discussed in Section 13.2.1, and it is such translations that limit the hard-sphere CSL model from accurately describing the energies of grain boundaries. Thus, to fully understand the correlation between the structure and energy of high-angle grain boundaries, it has been necessary to employ extensive atomistic calculation, as described in Section 13.2.4. The CSL theory does provide a simple and useful geometric mod-

Table 13.2. Some axis-angle pairs for CSL boundaries in the cubic lattice system

Θ^0	Σ
<100> Axis	
22.62	13a
28.07	17a
36.87	5
53.13	5
61.93	17a
67.38	13a
112.62	13a
118.07	17a
126.87	5
143.13	5
151.93	17a
157.38	13a
<110> Axis	
26.53	19a
38.94	9
50.48	11
70.53	3
86.63	17b
93.37	17b
109.47	3
129.52	11
141.06	9
153.47	19a
<111> Axis	
27.80	13b
38.21	7
46.83	19b
60.00	3
73.17	19b
81.79	7
92.20	13b
147.80	13b
158.21	7
166.83	19b
180.00	3
<210> Axis	
48.19	15
73.40	7
96.38	9
131.81	3
180.00	5
<211> Axis	
62.96	11
78.46	15
101.54	5
135.58	7
180.00	3
<221> Axis	
61.93	17b
90.00	9
112.62	13b
143.13	5
180.00	9
<310> Axis	
76.66	13b
93.02	19a
115.38	7
144.90	11
180.00	5
<311> Axis	
50.70	15
67-11	9
95.74	5
117.82	15
146.44	3
180.00	11
<320> Axis	
71.59	19b
100.48	11
121.97	17b
149.00	7
180.00	13a
<321> Axis	
86.18	15
123.75	9
150.07	15
180.00	7
<322> Axis	
107.92	13a
152.73	9
180.00	17b
<331> Axis	
63.82	17b
82.16	11
110.92	7
154.16	5
180.00	19a
<332> Axis	
99.08	19a
133.81	13a
180.00	11
<410> Axis	
107.92	13b
152.73	9
180.00	17a
<411> Axis	
93.37	17a
129.52	11
153.47	19b
180.00	9
<421 > Axis	
113.58	15
155.38	11
<430> Axis	
118.07	17b
157.38	13b
<431> Axis	
137.17	15
180.00	13b
<432> Axis	
121.76	19a
158.96	15
<433> Axis	
142.14	19a
180.00	17b
<441> Axis	
160.25	17a
<51O> Axis	
137.17	15
180.00	13a
<511> Axis	
73.17	19a
92.20	13a
120.00	9
158.21	7
<520> Axis	
121.76	19b
158.96	15
<521> Axis	
139.88	17b
180.00	15
<522> Axis	
160.25	17b
<530> Axis	
142.14	19b
180.00	17a
<531> Axis	
99.59	15
126.22	11
160.81	9
<532> Axis	
180.00	19b
<533> Axis	
105.35	17a
130.83	13b
162.66	11
<551> Axis	
110.01	19b
134.43	15
164.06	13a
<553> Axis	
137.33	17a
165.16	15
<610> Axis	
161.33	19a
161.33	19a
<611> Axis	
180.00	19a
<711> Axis	
110.01	19a
134.43	15
164.06	13b
<731> Axis	
137.33	17b
165.16	15
<733> Axis	
139.74	19b
<751> Axis	
166.83	19a

Source: Data from [24] and [47].

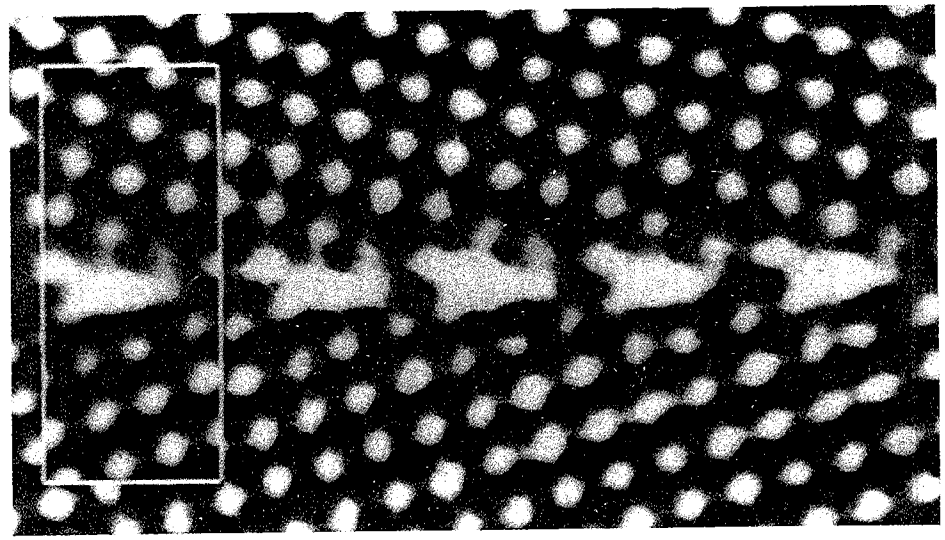

Figure 13.20. HRTEM image of a $\Sigma = 5$ grain boundary in nickel oxide viewed parallel to the <001> tilt-axis. A digitally averaged image in the inset shows a representative structural unit of the boundary, which is slightly asymmetrical. Reprinted from [48] with additional permission from Argonne National Laboratory.

el for understanding interfacial structure in terms of atom matching and mismatching between two crystals across the interface for any degree of misorientation, and it has been used extensively in describing the dislocation structure of solid–solid interfaces with considerable success.

Any lattice vectors of the CSL are solutions $\mathbf{x}^{(O)}$ of the O-lattice equation (Eq. 13.22) because at each independent site the rotational displacements between the two lattices amount to a lattice translation $\mathbf{b}^{(L)}$. However, not all O-lattice vectors $\mathbf{x}^{(O)}$ are CSL vectors. This point is illustrated by the complete O-lattice for the $\Sigma = 5$ boundary shown in Figure 13.19d. When the orientation between the two lattices is not exactly equal to that necessary for a CSL, all the coincident sites (except the center of rotation) are lost. In contrast, the O-lattice is still maintained with lattice vectors $\mathbf{x}^{(O)}$, which are now irrational although close to the rational CSL vectors. Thus, the O-lattice changes continuously between the discrete CSLs.

Displacement Shift Complete Lattice Geometrically, high-angle grain boundaries can be treated as small deviations from the nearest CSL. They are then similar to low-angle grain boundaries, where small deviations from the perfect single crystal (i.e., $\Sigma = 1$ CSL) are accommodated by lattice dislocations. Any deviation from a CSL is accommodated by lines of high local distortion or dislocations in between regions of undistorted CSL. In the case of low-angle grain boundaries, the dislocations are usually called primary dislocations and the boundary between them

is perfect crystal ($\Sigma = 1$). In the case of high-angle grain boundaries, the dislocations are called secondary dislocations and the boundary between them is perfect CSL.

The displacement shift complete (DSC) lattice defines the possible Burgers vectors of secondary dislocations [49]. These are perfect grain boundary dislocations that conserve the structure of the optimal coincidence orientation boundary. The DSC lattice acquired its name because it is a lattice of pattern-conserving displacements (i.e., a displacement of one crystal with respect to the other by a DSC vector restores the dichromatic pattern but with shifted coincidence sites). Thus, it causes a pattern shift that is complete. This feature is illustrated with reference to the $\Sigma = 5$ CSL in Figures 13.19e and f. In Figure 13.19e, the DSC lattice was constructed by defining the coarsest lattice that contains all of the sites of crystals 1 and 2 in the coincidence orientation as sublattices. The DSC lattice is indicated by the fine square mesh in this figure. Note that the DSC lattice points are not all translationally equivalent in the surroundings of crystals 1 and 2. When lattice 1 is shifted by the DSC vector indicated by an arrow in Figure 13.19f, the dichromatic pattern of the lattices is restored, but the resulting CSL (solid line) is shifted from its original position (dashed line).

The utility of the DSC construction is that any misorientation from the perfect $\Sigma = 5$ CSL orientation can be accommodated by these secondary dislocations with areas of perfect $\Sigma = 5$ boundary in between. The secondary dislocations thus occur when the primary dislocations are so close that they are not physically separate. The DSC dislocations then accommodate the irregularity in the periodicity of the primary dislocations, similar to the situation previously illustrated in Figure 13.6 using only primary dislocations. The secondary grain boundary dislocations required to accommodate the small misorientation from the exact CSL can be described by an equation equivalent to Eq. (13.12a) for low-angle boundaries, or

$$\mathbf{B}_s = (\mathbf{x} \times \mathbf{q})\, 2 \sin(\theta_{CSL}/2), \tag{13.27}$$

where $\mathbf{B}_s$ is the net Burgers vector content of the secondary grain boundary dislocations intercepted by any vector $\mathbf{x}$ lying in the plane of the boundary, and θ_{CSL} is the angular departure from the exact CSL orientation about an axis $\mathbf{q}$ common to one of the grains and the CSL. An important property of Eq. (13.27) is that it does not suffer from the ambiguity in the uniqueness of the Burgers vectors discussed for Eq. (13.12a). Equation (13.27) gives a unique value for the net Burgers vector $\mathbf{B}_s$ of the secondary grain boundary dislocation network because it is a property of the intersection of the translational symmetry elements of the two crystals and this is unique.

Formally, the DSC lattice can be defined as the lattice of difference vectors (i.e., vectors linking the lattice sites of crystal 1 to crystal 2), between lattices 1 and 2 in the exact coincidence orientation. Analytically, this can be expressed as

$$\mathbf{d}^{(DSC)} = \mathbf{x}^{(2)} - \mathbf{x}^{(1)} = (\mathbf{I} - \mathbf{A}^{-1})\mathbf{x}^{(2)}, \tag{13.28}$$

where $\mathbf{d}^{(DSC)}$ is a DSC lattice vector and the other symbols have the same meaning as in Eqs. (13.21) and (13.22). Another way of finding DSC vectors is to note that the DSC lattice for two direct lattices 1 and 2 is the reciprocal lattice of the CSL formed by the reciprocal lattices of 1 and 2 for the same axis and angle of rotation [50]. The reciprocal relation between the CSL and DSC lattices means that as Σ increases the primitive DSC vectors decrease in magnitude. Equation (13.28) can be solved graphically if Σ is not too high by drawing the two lattices in the coincidence orientation and position and finding the DSC vectors by inspection, as in Figure 13.19e. In this case, the lattice vectors of the DSC lattice are given as

$$1/10[310]_1,$$

$$1/10[\bar{1}30]_1 \text{ and}$$

$$1/10[21\bar{5}]_1.$$

Otherwise, the DSC vectors must be found analytically.

Schober and Balluffi [34] were the first investigators to provide strong experimental evidence for the CSL model of grain boundary structure by demonstrating that secondary grain boundary dislocations accommodated departures from CSL orientations. Their original results on twist boundaries in gold as well as those obtained in subsequent investigations are summarized in Figure 13.21. This figure shows the variation in dislocation spacing with twist angle θ for both primary and secondary grain boundary dislocations. The spacing D_{si} of the secondary grain boundary dislocations in the crossed grids varied with angular departure θ_{CSL} from each of the exact CSL orientations according to the same relationship given for primary dislocations in Eq. (13.2b), or

$$D_{si} = |\mathbf{b}_{si}|/\theta_{CSL}, \tag{13.29}$$

where $\mathbf{b}_{si}$ is the Burgers vector of the ith secondary grain boundary dislocation. The Burgers vectors that were found to satisfy Eq. (13.29) were the basis DSC vectors that were compatible with the line directions of the screw dislocations. Thus, for the near $\Sigma = 5$, $\Sigma = 13$ and $\Sigma = 17$ boundaries, the Burgers vectors found for the secondary grain boundary dislocations were of the type 1/10<310>, 1/26<510> and 1/34<530>, respectively. In addition, for the case of the near $\Sigma = 5$ boundaries, the Burgers vectors were found to agree with the contrast observed in TEM images of the interfaces, as illustrated in Figure 13.22. Note the weak contrast of the dislocations due to their small Burgers vectors as compared to Figure 13.12a.

It is important to note that the DSC lattice contains both lattices 1 and 2 in the coincidence orientation and position as sublattices. Therefore, it is continuous across any grain (or interphase) boundary and provides a suitable reference lattice on which Burgers circuits may be drawn [52]. This is an important point since various defects, such as ledges, occur at grain and interphase boundaries, and we need a method to quantify the nature of these defects. Thus, we now examine the character

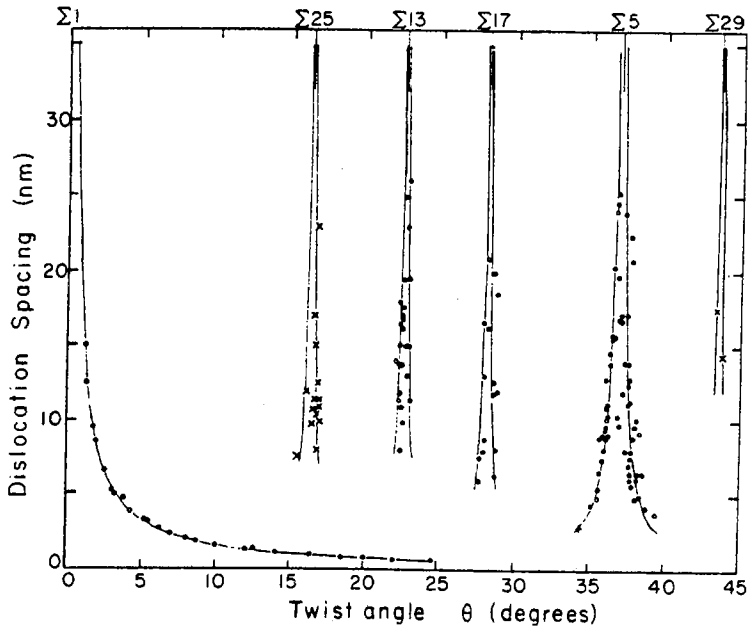

Figure 13.21. Variation of dislocation spacing with twist angle for primary and secondary grain boundary dislocations in gold. From [33] and [34,51] copyright Taylor & Francis Ltd.

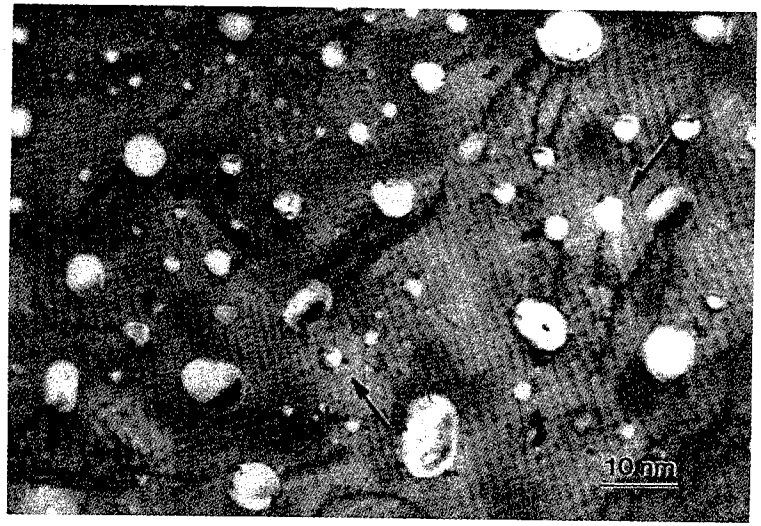

Figure 13.22. TEM image showing a cross-grid of secondary grain boundary dislocations in a near Σ = 5 (001) twist boundary in gold. From [34] copyright Taylor & Francis Ltd.

of ledges in grain boundaries using the DSC lattice as our reference lattice. This is followed by extension of the CSL/DSC construction to interphase boundaries.

Structure and Properties of Grain and Interphase Boundary Line Defects The topology of line defects that exist in grain boundaries in cubic materials is readily established within the framework of the DSC model [52,53]. The most general type of line defects possess both dislocation and ledge character, which can be defined by the Burgers vector **b** and the ledge vector **s**, respectively. (The term "step" is often used instead of "ledge" in the literature, but we use the term ledge to indicate its similarity with the ledges discussed in Parts II and III.) Possible line defects therefore include those with both dislocation and ledge character and special ones which are either pure dislocations or pure ledges. In addition, the line defects may be classified as intrinsic when they represent an integral part of the equilibrium boundary structure and extrinsic when they represent extra defects superimposed on the equilibrium structure. We mainly consider intrinsic defects.

If the dislocation character of a line defect is that of a perfect grain boundary dislocation, then the Burgers vector must be that of the DSC lattice, because this is composed of all lattice translation vectors of lattice 2 with respect to lattice 1 that conserve the atomic (dichromatic) pattern. The ledge vector then corresponds to a shift in space of the above pattern, which occurs when lattice 2 is translated with respect to lattice 1 by the Burgers vector. These ledge vectors are always vectors of the crystal lattices and therefore also of the DSC lattice. The topological properties of these line defects in grain boundaries can be revealed with the DSC framework using the examples shown in Figure 13.23.

In Figure 13.23, the Burgers vector of the dislocation is seen to be a vector of the DSC lattice as are ledge vectors $\mathbf{s}_1$ and $\mathbf{s}_2$ in lattices 1 and 2, respectively. The Burgers vector of the defect on the left can be readily obtained by constructing a Burgers circuit using the DSC lattice as the reference lattice as described by Hirth and Balluffi [52]. The Burgers vector and ledge vectors are related by

$$\mathbf{b} = \mathbf{s}_1 - \mathbf{s}_2. \tag{13.30}$$

The heights of the ledges in the boundary plane (with their appropriate signs) are given by $\mathbf{s}_1 \cdot \mathbf{n}$ and $\mathbf{s}_2 \cdot \mathbf{n}$ for lattices 1 and 2, respectively, where $\mathbf{n}$ is a unit vector normal to the boundary plane and pointing from crystal 1 into crystal 2. In Figure 13.23, $\mathbf{s}_1 \cdot \mathbf{n} = \mathbf{s}_2 \cdot \mathbf{n}$ and the effective ledge height produced by the line defect in the relaxed boundary structure is given by $\mathbf{s}_1 \cdot \mathbf{n} = \mathbf{s}_2 \cdot \mathbf{n}$. When $\mathbf{s}_1 \cdot \mathbf{n} \neq \mathbf{s}_2 \cdot \mathbf{n}$, the effective ledge height may be taken as $1/2(\mathbf{s}_1 + \mathbf{s}_2) \cdot \mathbf{n}$.

A line defect that is a pure ledge without dislocation character is obtained in the special case when $\mathbf{s}_1 - \mathbf{s}_2 = \mathbf{b} = 0$. An example is the pure ledge at *AB* in Figure 13.23, where $\mathbf{s}_1 = \mathbf{s}_2$ is a vector of the CSL. Conversely, a line defect that is a pure grain boundary dislocation without ledge character is obtained in the special case when $\mathbf{s}_1 \cdot \mathbf{n} = \mathbf{s}_2 \cdot \mathbf{n} = 0$. An example would be a grain boundary dislocation lying in a boundary plane parallel to the VWUT plane of the CSL shown in Figure 13.23, possessing the same Burgers vector **b** as the dislocation shown at *C*.

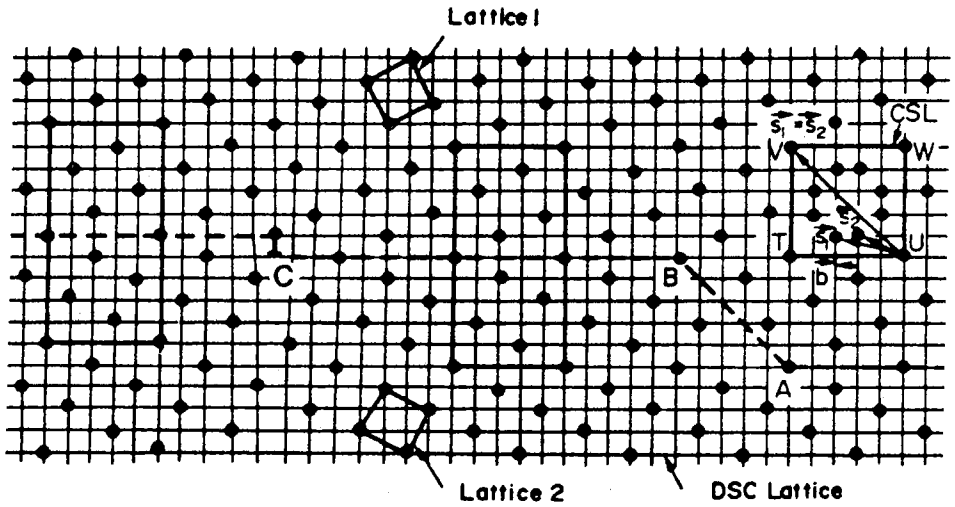

Figure 13.23. Line defects in a $\Sigma = 5$ symmetrical-tilt boundary produced by 36.9° rotation around [001]. A line defect possessing both dislocation and ledge character is shown on the left at *C* and a pure ledge is shown at *AB*. The Burgers vector and ledge vectors of the two line defects are shown in the diagram in the upper right. Reprinted with permission from [53] by Elsevier Science Ltd., Oxford, England.

These line defects possess a number of important topological properties summarized below.

1. Movement in the plane of the boundary of a line defect that possesses a dislocation character (which may require glide and climb) causes lattice 2 to translate with respect to lattice 1.
2. Movement of a line defect that possesses a ledge character causes the interface to translate with respect to lattices 1 and 2.
3. Climb of line defects possessing a dislocation character allow the boundary to act as a source or sink for point defects.
4. Lattice dislocations $\mathbf{b}^{(L)}$ that impinge on the boundary may dissociate into an integral number of grain boundary line defects $\mathbf{b}_i$ because the Burgers vectors of the lattice dislocations and the interfacial dislocations are all vectors of the DSC lattice and must obey the conservation relation $\mathbf{b}^{(L)} = n_i\mathbf{b}_i$, where n_i is the number of grain boundary dislocations of type i.
5. Lattice dislocations that cut through a boundary leave behind a line defect with dislocation character possessing a Burgers vector given by the DSC lattice.

The description of line defects in a grain boundary (homophase interface) by the DSC lattice can be readily extended to general heterophase interfaces. The details of this construction have been thoroughly discussed [53,54]. We examine only the end results to show that dislocations and ledges in general heterophase boundaries can be analyzed within the same DSC framework developed for grain boundaries above. This construction provides a convenient way to quantify the character of line defects at heterophase interfaces in much the same way that we quantify the Burgers vectors of lattice dislocations [39].

Figures 13.24 and 13.25 show semicoherent planar and inclined interphase interfaces between two lattices (phases), respectively. The lattices can be assumed to be related by the transformation matrix **A** in Eq. (13.18). The vectors **b**, $\mathbf{s}_1$ and $\mathbf{s}_2$ in these figures have the same meanings as in Figure 13.23. The cells indicated as M_1 and M_2 in the figures identify a pair of cells in the strain free lattices (phases) 1 and 2, which almost match each other in both size and shape. These cells are usually, but not always, sublattices of the respective crystal lattices. The fine lines in the figures indicate the DSC lattice formed from lattices 1 and 2 in the same way as in Figures 13.19e and 13.23.

The line defects in the general interfaces have basically the same dislocation and ledge features as their counterparts in the special case of grain boundaries in cubic materials discussed previously. The ledge vector **s** is defined in the same way and for the defects in the boundary illustrated in Figure 13.24, $\mathbf{s}_1 \cdot \mathbf{n} = \mathbf{s}_2 \cdot \mathbf{n} = 0$. These line defects are therefore interfacial dislocations without any ledge character and a Burgers vector **b** defined by the DSC lattice between M_1 and M_2. They are of-

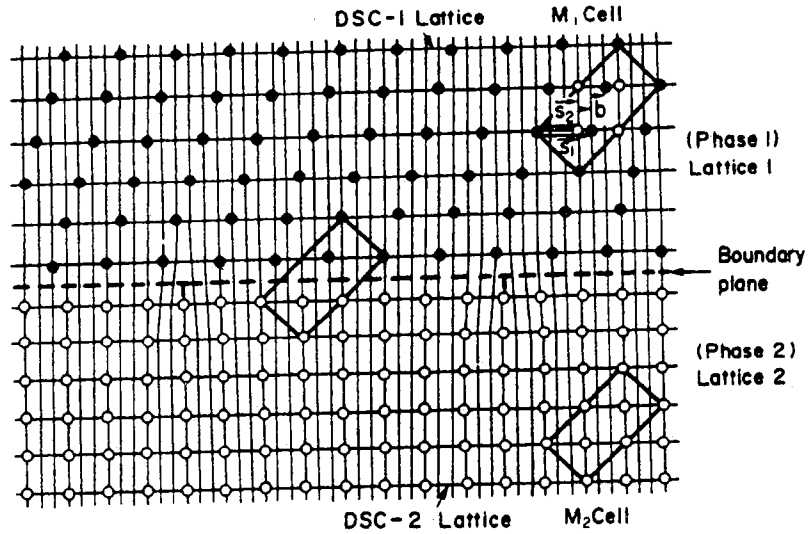

Figure 13.24. The interphase boundary between two different lattices (phases) M_1 and M_2, which form a planar interface containing interfacial dislocations with a spacing determined by O-lattice theory. The Burgers vector and ledge vectors of the interfacial dislocations are shown in the diagram in the upper right. The DSC lattice is indicated by fine lines in the figure. Reprinted with permission from [53] by Elsevier Science Ltd., Oxford, England.

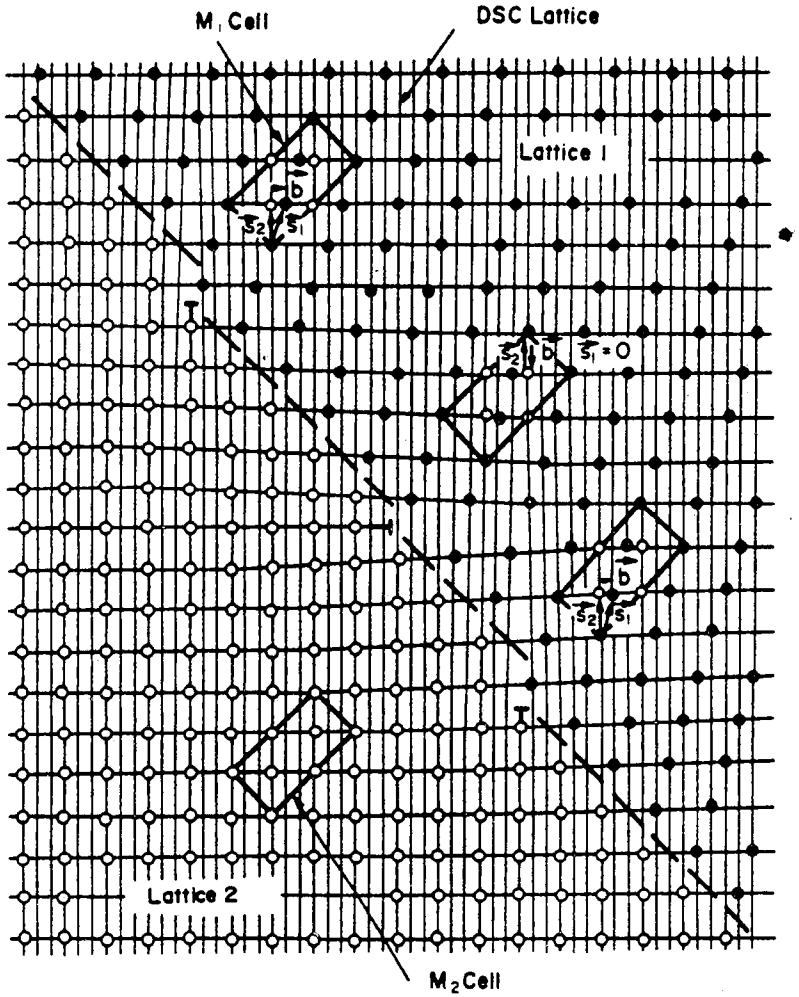

Figure 13.25. An interphase boundary between lattices 1 and 2 in Figure 13.24, but with the boundary plane at a different inclination. Two types of line defects are present possessing both dislocation and ledge character. The Burgers vectors and ledge vectors are illustrated in each case. Reprinted with permission from [53] by Elsevier Science Ltd., Oxford, England.

ten referred to as misfit dislocations, and this is a typical semicoherent interface [1] as illustrated previously in Figure 7.7 and Figure 12.5. In the general case, the line defects will have both dislocation and ledge character as seen in Figure 13.25, where a boundary is shown that differs from the boundary in Figure 13.24 only by a rotation of the interface plane. In this case, $\mathbf{s}_1 \cdot \mathbf{n} \neq \mathbf{s}_2 \cdot \mathbf{n} \neq 0$ for one type of line defect (indicated by ⊤) and $\mathbf{s}_1 = 0$ and $\mathbf{s}_1 \cdot \mathbf{n} \neq 0$ for the other (indicated by ⊣). A ledge is therefore evident at each defect. Note that unlike the atom positions around

the two dislocations in Figure 13.24 where a terminating plane is evident, the atom planes are completely coherent around the ledges (indicated by ⊤) for which $\mathbf{s}_1 \cdot \mathbf{n} \neq 0$. Such defects are commonly found at high-index interfaces in both martensitic [6] and diffusional [16] solid–solid transformations and are often referred to as transformation dislocations or structural ledges [1,55,56] depending on their role in the interface. The ledges in Figure 12.7 possess this type of defect character.

It is also possible to have pure interphase boundary ledges without DSC lattice dislocation character, as shown in Figure 13.26, where a pure ledge has been inserted in the boundary shown previously in Figure 13.24. In this case, $\mathbf{s}_1 = \mathbf{s}_2$ and $\mathbf{b} = \mathbf{s}_1 - \mathbf{s}_2 = 0$, although in the DSC lattice framework the ledge may have an associated weak, long-range stress field if isolated in the boundary without complete relaxation by other DSC lattice dislocations in the interface, as apparent in the figure [53]. Because the line defects in general interphase boundaries have basically the same dislocation and ledge features as their counterparts in grain boundaries in cubic crystals, we expect them to possess the same basic topological properties summarized previously for grain boundaries.

In summary, the DSC lattice framework is general and it provides a means of quantifying the various types of line defects found in grain and interphase boundaries in materials. In many cases, the DSC lattice can be obtained by simple graphical construction based on the atomic positions in the structures, as in the examples shown here. The Burgers vectors and ledge vectors of interfacial line defects can then be obtained directly from the construction. In cases where graphical construction is difficult, the problem can be solved by computer techniques. The main limitations of the DSC method are that (a) it is a geometric hard-sphere construction

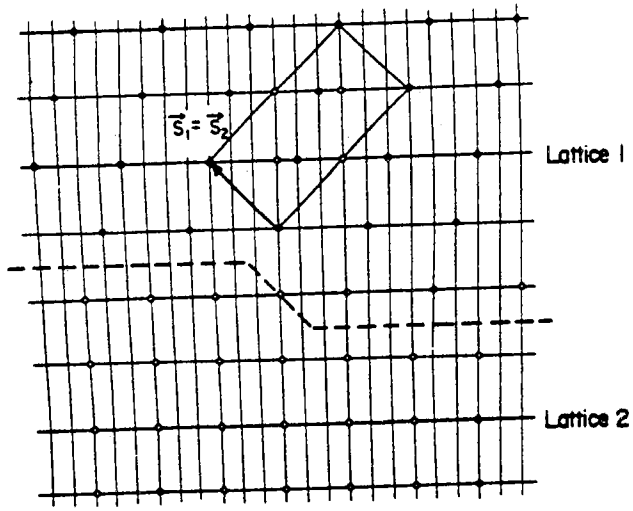

Figure 13.26. Pure ledge in the interphase boundary illustrated previously in Figure 13.24. The ledge vectors are shown above the ledge. Reprinted with permission from [53] by Elsevier Science Ltd., Oxford, England.

and thus unable to account for local atomic relaxations that can occur at interfaces, and (b) it represents an approximation in near-coincidence situations when there are two different types of lattices, as in Figure 13.24, for example. In spite of these limitations, it is easy to apply and useful for analyzing many different types of interfaces.

Before ending this section, it is worth noting that Pond [57,58] has developed a method for quantifying the nature of line defects in interfaces based on the space group symmetries of the adjacent crystals. This method is completely general and does not suffer from the limitations of the hard-sphere models above in its capability to quantify the character of interfacial defects. Because a thorough knowledge of space group crystallography is required to utilize this technique, it is not discussed in this book. However, it is highly recommended as additional reading for those familiar with space group notation. Several other approaches to the determination of grain boundary structure that have been developed are not mentioned here, because they are not critical to our discussion and they are summarized elsewhere [24,33,42,59].

13.2.4. Atomistic Modeling of Grain Boundary Structure and Energy

The main purpose of atomistic investigations of grain boundary structure is to relate the structure and grain boundary energy γ_{gb} to the grain misorientation and boundary plane. The calculations are usually performed by establishing an initial relationship between two grains using the five macroscopic degrees of freedom discussed in Section 13.2.1. An atomic potential is chosen and the bicrystal is then allowed to relax into a minimum energy configuration through a suitable algorithm, as discussed in Section 1.3 [7,60]. Relative translations of the two lattices through the three microscopic degrees of freedom and/or local atomic rearrangements are all allowed as part of the minimization process. Initially, there was some question as to the validity of the interatomic potentials used in the calculations, the approximations used to reach equilibrium and whether calculated energy minima corresponded to real energy minima, but these uncertainties have been largely relieved by extensive comparison between calculated and observed grain boundary structures [2,7].

Two important fundamental insights have arisen from calculations of the structure and energies of grain boundaries in metals. Firstly, it has been shown that the structure of grain boundaries can be described as composed of several structural (or polyhedral) units, which are repeated in a particular sequence along the boundary, depending on the type of boundary and angle of misorientation. This result is appealing because of its conceptual simplicity and because it relates to certain properties of boundaries such as nearest-neighbor bonding, segregation and diffusion. Secondly, it has been shown that the grain boundary energy is directly correlated with the volume expansion of the boundary per unit area and that this feature relates to the nearest-neighbor hard-sphere character of the atoms. These studies have also elucidated the reason why the CSL model does not accurately predict the energies of grain boundaries except in special orientations. Each of these subjects is exam-